RESEARCH ARTICLE

VOLCANICA

Improving magmatic CO_2 reconstruction using X-ray Computed Tomography to accurately quantify melt inclusion volumes and geometries

Helen R. Thornhill *[α], David J. Ferguson[α], Alice Macente[β,γ], Felix O. Boschetty[δ, ε], Eduardo Morgado[ζ], and Jason Harvey[α]

[α] School of Earth and Environment, University of Leeds, Leeds, UK.
[β] School of Civil Engineering, University of Leeds, Leeds, UK.
[γ] Department of Earth Sciences, University of Florence, Florence, Italy.
[δ] Department of Earth Sciences, University of Manchester, Manchester, UK.
[ε] Department of Earth Sciences, University of Oxford, Oxford, UK.
[ζ] Escuela de Geologia, Universidad de Mayor, Santiago, Chile.

Submitted: 2025-05-02 | Accepted: 2026-02-09 | Published: 2026-02-11

Editor: J. Farquharson | Typesetter: J. Farquharson

Abstract

Melt inclusions provide a critical archive of primary magmatic compositions, particularly for reconstructing volatile systematics that are otherwise obscured by syn-eruptive degassing. Accurate quantification of volatile species such as CO_2 requires robust determination of both melt and vapour bubble volumes within polyphase inclusions. Conventional 2D optical measurements impose simplified geometries and assumptions, introducing significant and often unquantifiable errors. Here we demonstrate that X ray Computed Tomography (XCT), a non destructive, high resolution 3D imaging technique, provides substantially more accurate and reproducible melt inclusion and bubble volume measurements across a large dataset of olivine hosted inclusions. Comparison with traditional methods reveals that 2D approaches can overestimate bubble volumes by 14–40%, with errors expected to rise substantially in inclusions with complex morphology. XCT not only improves volumetric accuracy but also enables explicit uncertainty evaluation through repeat scanning and variable image processing. These advancements significantly enhance CO_2 reconstructions and thereby refine estimates of magmatic volatile budgets, storage depths, and magmatic compositions.

Non-technical summary

Melt inclusions are small pockets of magma trapped within growing crystals, preserving otherwise inaccessible information about magmatic conditions and compositions at depth. These inclusions often contain dissolved volatile species, including CO_2, that can exsolve into a vapour bubble. Accurate reconstruction of total CO_2 contents requires reliable measurements of both inclusion glass and bubble volumes. Traditionally, 2D optical methods are used to quantify volumes, assuming simple ellipsoidal geometries. This introduces substantial uncertainties, particularly when inclusions have more complex shapes. This study demonstrates that X ray Computed Tomography (XCT) provides a viable and valuable alternative, producing high quality three dimensional images of melt inclusions. These enable direct determination of true inclusion and bubble geometries, and associated uncertainties. XCT also allows for efficient processing of large datasets and avoids destructive sample preparation. Incorporating XCT into melt inclusion studies significantly improves volume estimates and, consequently, the accuracy of CO_2 reconstructions. This enhanced precision supports more robust interpretations of volatile cycling, magma storage depths, and the conditions under which magmas evolve within volcanic systems.

Keywords: Melt Inclusions; X-Ray Computed Tomography; CO_2; 3D Volumes; Magmatic Volatiles; Barometry.

1 Introduction

Melt inclusions, small droplets of silicate melt trapped within crystals, are a valuable petrological tool used widely in studies of magmatic processes [Anderson 1976; Roedder 1979; Lowenstern 1995; 2003; Rose-Koga et al. 2021; Wallace et al. 2021]. They provide a unique opportunity to sample otherwise inaccessible melts from within a magmatic system, preserving primitive magma compositions and dissolved volatile species that are otherwise lost during magma evolution, mixing, ascent, and degassing [Roedder 1979; Cannatelli et al. 2016; Wallace et al. 2021].

Primary melt inclusions are generally accepted to form during crystal growth, due to a small droplet of melt adhering to the surface of a growing crystal [Roedder 1979]. This likely occurs due to irregularities in growth conditions such as rapid skeletal growth, dissolution and crystal regrowth, or as the result of the attachment of an immiscible phase to the growing crystal edge [Roedder 1979; Welsch et al. 2014; Wallace et al. 2021]. As the crystal continues to grow, the adhering droplet becomes fully enclosed, resulting in a melt inclusion that is largely isolated from subsequent physicochemical changes in the host magma body [Lowenstern 2003].

Many studies have utilised melt inclusions to provide insights into the architecture and dynamics of magmatic systems, constraining processes such as magma generation, crystallisation and fractionation, mixing, contamination, pre-eruptive volatile contents, and storage pressures [Anderson 1976; Jackson and Hart 2006; Rose-Koga et al. 2012; Mann

* ee18hrt@leeds.ac.uk

et al. 2013; Barker et al. 2020; Wieser et al. 2021; Esposito et al. 2023]. The determination of pre-eruptive volatile contents (CO_2, H_2O, S, Cl etc.), has been particularly impactful on the study of volcanic systems and geological volatile cycles (e.g. [Lowenstern 1995; 2003; Wallace 2005; Metrich and Wallace 2008; Hartley et al. 2014; Miller et al. 2019; Plank and Manning 2019; Allison et al. 2021; Feignon et al. 2022].

1.1 Reconstructing magmatic CO_2 contents from melt inclusions

A key goal for many volcanic studies is the quantification of magmatic CO_2, facilitated by the study of melt inclusion volatile contents. Accurate determination of inclusion CO_2 contents is critical for applications such as magma storage depth investigation via inclusion barometry [Anderson 1976; Wieser et al. 2021], understanding pre-eruptive dissolved volatile and gas contents of magmas [Hartley et al. 2014; Allison et al. 2021; Feignon et al. 2022], and constraining the magmatic flux of deep earth volatiles and cycling at subduction zones [Miller et al. 2019; Plank and Manning 2019; Wong et al. 2019; Lopez et al. 2023]. The solubility of CO_2 in basaltic melts is strongly dependent on pressure, with most magmas almost entirely degassed by the time they are erupted at the surface [Anderson 1976; Pan et al. 1991; Shishkina et al. 2014]. Melt inclusions provide access to magmas that were trapped before complete CO_2 exsolution. This thereby allows the constraint of the CO_2 budget of magmatic systems and magma storage depths via melt inclusion barometry, usually in combination with H_2O data [Anderson 1976; Lowenstern 1995; 2003; Mann et al. 2013; Wieser et al. 2021].

Melt inclusions can form in any magmatic mineral, however, most studies target olivine. This is due to its near ubiquity in basaltic and basaltic-andesite magmas, well-established elemental partitioning and diffusion behaviours, and the high likelihood of capturing inclusions of primitive melts as an early-crystallising magmatic phase [Danyushevsky et al. 2000; Danyushevsky et al. 2002; Rasmussen et al. 2020; Wallace et al. 2021]. Inclusions can range in size and shape, but are usually between 50–250 µm. They may undergo post-entrapment modifications (PEM), such as the formation of one or more bubbles, internal crystallisation or devitrification of the inclusion glass, crystallisation of the host mineral onto the inclusion walls or 'necking' where joined inclusions may be cut off from each other, diffusive exchanges of Fe-Mg with the host crystal, and diffusive loss of H_2O [Danyushevsky et al. 2000; Danyushevsky et al. 2002; Newcombe et al. 2014; Maclennan 2017; Yao et al. 2020; Brahm et al. 2021; Wallace et al. 2021]. These modifications must be accounted for to correctly reconstruct magmatic compositions and volatile contents from inclusions. In general, to reduce the necessity for extensive corrections, studies target large, glassy melt inclusions that have been quenched rapidly and are therefore relatively chemically homogeneous.

Dissolved volatile contents in melt inclusion glass and composition can be determined by a variety of microanalytical techniques, including Secondary Ionisation Mass Spectrometry (SIMS) or Fourier Transform Infrared Spectroscopy (FTIR). Many naturally glassy melt inclusions also contain one or more vapour bubbles (often termed as shrinkage bubbles), which must also be taken into account. These form from the post-entrapment exsolution of volatiles within an inclusion as a result of the reduction of internal pressures, often due to differential thermal contraction of the host crystal and melt along with other PEM processes [Lowenstern 2003; Moore et al. 2015; Rasmussen et al. 2020]. Such bubbles are very common in glassy, olivine-hosted melt inclusions and typically contain a substantial fraction of the total inclusion CO_2 contents, in some cases >90 % [Moore et al. 2015; Wallace et al. 2015; Aster et al. 2016; Maclennan 2017; Rasmussen et al. 2020; Wieser et al. 2021]. In the last decade, the significance of the CO_2 content in inclusion bubbles has become widely recognised, therefore highlighting the necessity to measure CO_2 contents in both the glass and vapour phases of poly-phase inclusions. There is also emerging evidence that, in some cases, carbonate minerals precipitated on the bubble walls may play a key role in sequestering inclusion CO_2 [Venugopal et al. 2020; Buso et al. 2022; Feignon et al. 2022].

1.2 Bubble-bearing melt inclusions

There are a variety of methods that have been adopted to quantify the CO_2 budget of bubble-bearing melt inclusions [Lowenstern 2003; Wallace et al. 2015; Rose-Koga et al. 2017; Rasmussen et al. 2020]. Experimental homogenisation has been applied in multiple studies, allowing for eventual analysis of only the (homogenised) glass phase. This approach can be problematic, with difficulties associated with dissolving original bubbles and/or nucleation of new bubbles upon quenching [Mironov et al. 2015; Rasmussen et al. 2020]. Other difficulties with this method include the diffusive loss of H_2O during homogenisation, over dissolution of olivine on the inclusion walls, and the loss of petrological information such as mineral and inclusion zoning [Wallace et al. 2015; Rasmussen et al. 2020; Wieser et al. 2021; Buso et al. 2022]. Another approach is to calculate a theoretical bubble CO_2 content using equations of state (EOS), assuming melt-bubble chemical equilibrium before quenching [Anderson and Brown 1993]. This requires estimation of both the inclusion and bubble volume. The bubble volume is either estimated as an assumed proportion of the total inclusion or measured optically [Anderson and Brown 1993; Tucker et al. 2019]. While simple to apply, this approach can result in erroneously high CO_2 contents due to late-stage bubble expansion that can occur upon eruption with no concurrent CO_2 addition [Maclennan 2017; Rasmussen et al. 2020; Wieser et al. 2021].

An alternative method is the measurement of CO_2 density within the inclusion bubble via Raman Spectroscopy [e.g. Esposito et al. 2011; Hartley et al. 2014; Aster et al. 2016; Lamadrid et al. 2017; Mironov et al. 2020; Venugopal et al. 2020; Wieser et al. 2021; Feignon et al. 2022]. The density of CO_2-rich bubbles can be determined by measuring the distance between the two primary CO_2 peaks in Raman spectra (the Fermi diad). Peak separation is dependent on CO_2 density [Esposito et al. 2011; Aster et al. 2016; Lamadrid et al. 2017; Mironov et al. 2020]. The derived CO_2 density can then be converted into a CO_2 concentration (usually displayed in parts per million (ppm)), via mass balance between the bubble and

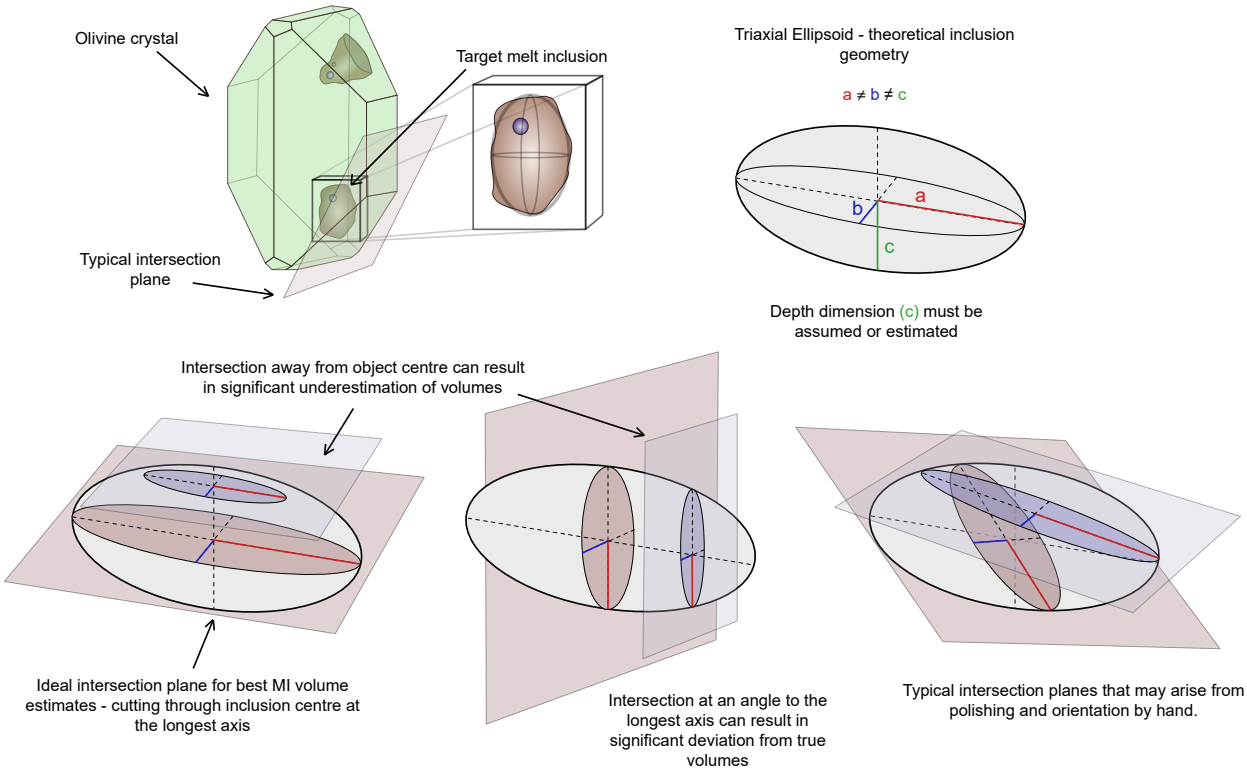

Figure 1: Schematic diagram showing an olivine crystal containing melt inclusions, along with ellipsoid intersection planes and the variety of 2D sections that these can produce. This introduces large errors and uncertainty into volumes estimated from two-dimensional measurements.

inclusion, requiring the volumes of both the glass (inclusion) and vapour (bubble) phases, and the density of the inclusion glass (Equation 1):

$$[CO_2]_{\text{bubble}}\ (\text{ppm}) = 10^6 \times \frac{(\rho_{CO_2\text{bubble}} \times V_{\text{bubble}})}{(\rho_{\text{melt}} \times V_{\text{melt}})}. \quad (1)$$

The total inclusion CO_2 can then be calculated by summing this with CO_2 concentration data from the inclusion glass, obtained by methods such as SIMS or FTIR. This technique has been successfully applied (using calibrated Raman instruments) in several recent inclusion studies [Lamadrid et al. 2017; DeVitre et al. 2021; Wieser et al. 2021; Van Gerve et al. 2024].

1.3 Estimating melt inclusion volumes

The determination of total melt inclusion CO_2 contents using Raman Spectroscopy or the EOS method requires accurate quantification of inclusion and bubble volume. In general, these volumes are estimated using two-dimensional measurements and the assumption of a simplified geometry, commonly ellipsoidal and spherical for the inclusion and bubble, respectively [Figure 1; Miller et al. 2019; Hanyu et al. 2020; DeVitre et al. 2023; Van Gerve et al. 2024]. The long and short axes of an ellipse or circle, fitted around an intersected inclusion and/or bubble, are measured using images obtained using optical microscopy or scanning electron microscopy (SEM). The third, depth dimension for the inclusion can then be estimated, assuming a simple three-dimensional geometry [Esposito et al. 2014; Hartley et al. 2014; Aster et al. 2016; Tucker et al. 2019; Wieser et al. 2021]. For the best volume estimation, the crystal should be oriented so that the longest inclusion axis is parallel to the polished surface; however, in reality, this can be difficult to control due to challenges associated with mounting and manipulating loose crystals (Figure 1). It is also possible to attempt to double polish crystals around the inclusion on two orthogonal surfaces to constrain the depth dimension [Mironov et al. 2020; DeVitre et al. 2023]. If multiple inclusions are exposed along the same surface, a compromise to the optimal intersection angle is likely to be necessary.

While commonly available and easily accessible, these conventional optical methods can lead to oversimplification of inclusion geometries, resulting in large volume errors [Tucker et al. 2019; Hanyu et al. 2020; Van Gerve et al. 2024]. They also require physical removal of material via polishing to expose and view inclusions. Often, this can result in the destruction of other inclusions and the host crystal to reach the target inclusion, removing spatial context for inclusion analysis. Very few inclusions reflect a perfect ellipsoidal shape, with degrees of faceting common along with other surface irregularities causing deviation from a true ellipsoidal geometry (Figure 1). In conjunction with geometrical oversimplification, variation in the angle of intersection and therefore measure-

ment has a considerable impact on these estimated volumes, with best estimates likely to overestimate ellipsoid volumes by around 40 % [Tucker et al. 2019]. Improvements can be made if a depth measurement is taken using a calibrated microscope and a double polished sample, focusing on the top and base of the inclusion, respectively [Mironov et al. 2020; DeVitre et al. 2023]. Double polishing can improve the viewing angle for more irregular shapes, but simplification to an ellipsoidal geometry will still considerably affect these estimates [Mironov et al. 2020; DeVitre et al. 2023]. These factors result in large, unquantifiable errors for melt inclusion volumes calculated using two-dimensional methods. When used in CO_2 calculations, these erroneous volumes substantially affect subsequent inclusion CO_2 determinations. It is becoming increasingly evident that better volume quantification methods are required, where real, three-dimensional inclusion geometries can be considered and uncertainties can be quantified [Miller et al. 2019; Tucker et al. 2019; Hanyu et al. 2020; DeVitre et al. 2023; Van Gerve et al. 2024; Jorgenson et al. 2025].

In this study, we demonstrate the use of X-Ray Computed Tomography (XCT) to determine the three-dimensional volumes of a large sample suite of melt inclusions and bubbles, hosted in volcanic olivine crystals. Geometrical and orientational data are also collected and evaluated to investigate inclusion characteristics and populations within crystals from a variety of volcanic eruptions. We demonstrate that XCT is a viable, and indeed valuable, tool for the study of melt inclusions and, in particular, can greatly improve the accuracy and precision of CO_2 reconstructions from bubble-bearing inclusions. While a handful of previous studies have applied this method to extract inclusion volumes for CO_2 reconstructions [Miller et al. 2019; Hanyu et al. 2020; Van Gerve et al. 2024], these have only used XCT for a small subset of inclusions or crystals (9 inclusions, 26 inclusions, and 15 crystals containing 133 inclusions, respectively). Here, we provide a basic workflow that can be adapted and applied to a large number of inclusions. We also include a method that can be applied to quantify the errors associated with this imaging technique and subsequent processing, so that this can be incorporated into future studies and their subsequent CO_2 reconstructions.

2 Methods

2.1 Sample selection and preparation

The inclusion-bearing olivine crystals in this study were selected from loose scoria samples collected from Mocho-Choshuenco, an arc volcano in Southern Chile. Mocho-Choshuenco volcanic complex has been frequently active since the last regional glaciation of Southern Chile and Patagonia (~18ka: [Hulton et al. 2002; Bertrand et al. 2008; Glasser et al. 2008; Fontijn et al. 2016; Alloway et al. 2022]. The volcano has produced a large volume of compositionally variable eruptions with notable differences in explosivity and eruption style, geochemical signatures, and signs of elevated CO_2 contents [McMillan et al. 1989; Rawson et al. 2015; 2016a; b; Feignon et al. 2022; Mallea-Lillo 2022; Moreno-Yaeger et al. 2024]. Samples for this study were collected from ten of the main post-glacial eruptive units, as defined in Rawson et al. [2015], with olivine crystals picked from loose scoria and pumice deposits. The units were chosen to sample a variety of eruption styles and compositions. Comparison of melt inclusion populations will facilitate the investigation of magma system dynamics that may influence eruptive style, such as volatile content and storage conditions.

Olivine crystals bearing large, glassy melt inclusions (where visible) were separated by hand to be prepared for imaging via XCT. In total, 147 crystals were selected with sizes ranging from 0.5–1.5mm, including a variety of crystal and inclusion morphologies. Of these, only the scans of 92 crystals have been processed for this study. This reduction is due to a range of factors affecting the suitability of the melt inclusions for subsequent volatile analysis. This was predominantly due to cracking of the crystals and inclusions, devitrification and crystallisation within the melt inclusions, and over-complexity of inclusion geometries and populations beyond the spatial resolution used in this study (i.e. inclusions too close to separate during processing, and thin connecting films/neck features). Only inclusions that would be viable and targeted for further geochemical analysis for volatile quantification were processed in this study.

Between 10–20 olivine crystals were mounted on the inside of a small plastic straw, secured with double-sided tape and photographed for reference and identification. The straw was then re-rolled and secured with tape (Figure 2A). Overall, sample dimensions of 3 × 3 mm (straw height × diameter) were chosen to obtain an ideal XCT spatial resolution of approximately 3 × 3 × 3 µm (voxel size). Higher spatial resolution is possible; however, this would require smaller sample sizes, limiting the number of crystals per scan, necessitating more scans and instrument time.

2.2 X-Ray Computed Tomography

X-Ray Computed Tomography (XCT) is a non-destructive technique that can provide three-dimensional imaging of the internal density structure of materials at micrometre to submicrometre resolution [Withers et al. 2021]. Previous studies have used this technique to image and quantify geological samples, including studies of fluid and melt inclusions [Nakashima et al. 1997; Cnudde and Boone 2013; Créon et al. 2018; Richard et al. 2019]. XCT uses the penetrative power of X-rays to produce three-dimensional models of objects, recording the signal of the X-rays as they are attenuated by the sample (X-ray attenuation coefficient) into photons of visible light. The X-ray attenuation within a heterogeneous sample varies as a function of the atomic number and density of the material [Cnudde and Boone 2013; Pankhurst et al. 2014]. There are various geometries of XCT systems. In this study, a cone-beam geometry was used, with the sample placed in the path of the X-ray beam on a rotating stage moving around 360°, multiple radiographs (or projections) were collected as the sample rotated (Figure 2A). These projections are then reconstructed to produce a three-dimensional model of the sample, where each pixel (or voxel in 3D) contains information about the attenuation coefficient, and therefore density of the sample [Cnudde and Boone 2013; Withers et al. 2021]. This three-dimensional dataset, constructed from voxels, is

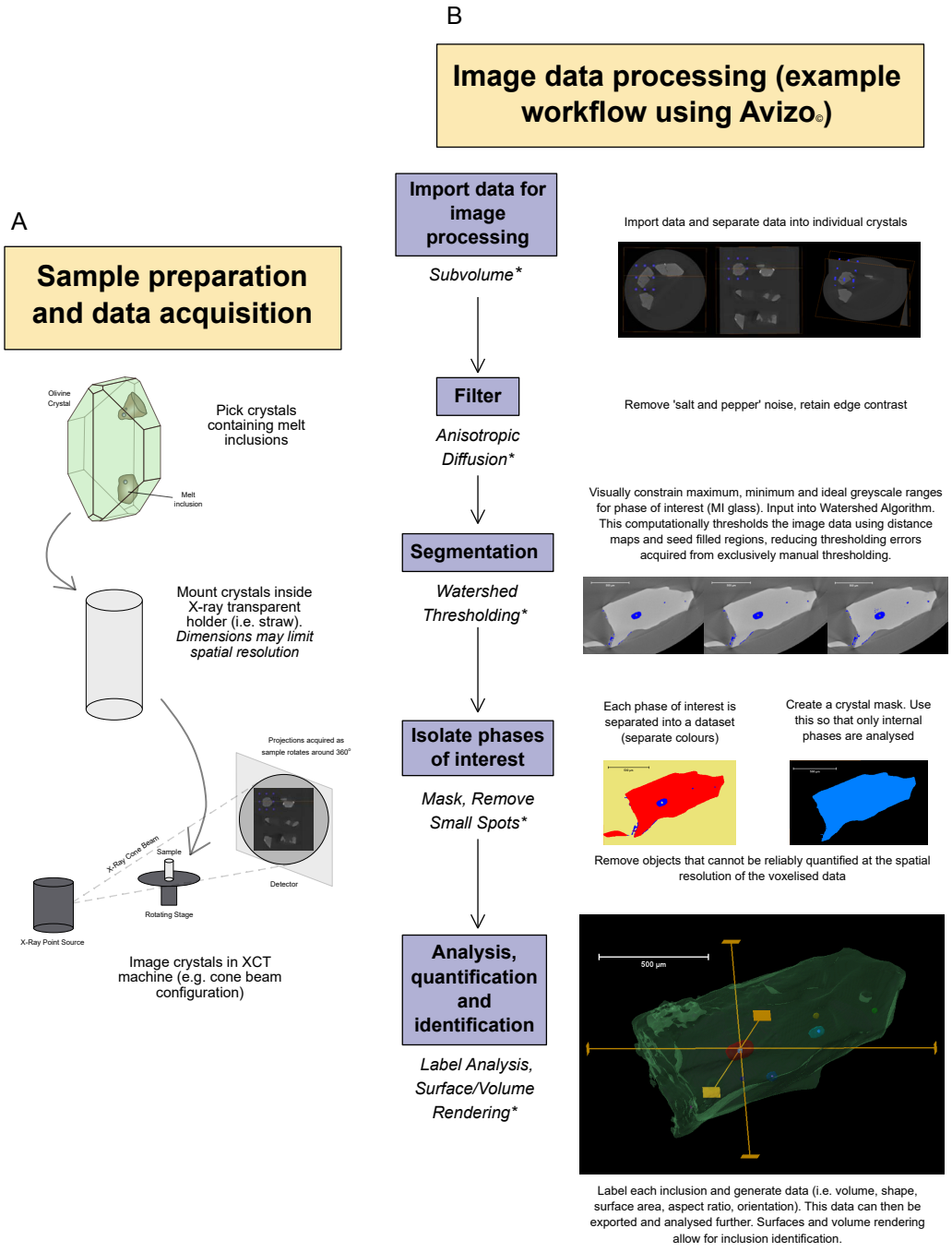

Figure 2: A generalised workflow showing the steps necessary to analyse olivine-hosted melt inclusions using XCT. [A] Schematic showing the general sample preparation process and a schematic of the instrumental setup for an XCT scanner. [B] A typical image processing workflow for use in the Thermo Scientific™ Avizo © image processing software, however, this can be adapted and applied to other software packages. The software-specific algorithms used in this study are marked with an asterisk (*) and are described in detail in Section 2.2 and Section 2.3. Also see Supplementary Material 1 (Figure S2) for an example processing workflow.

converted to greyscale values that represent the internal variation in X-ray linear attenuation coefficient, which can be processed to identify distinct phases (segmentation) [Nakashima et al. 1997; Schlüter et al. 2014; Lin et al. 2015]. The density contrast between olivine, silicate glass inclusions, and vapour bubbles causes sufficient variations in X-ray attenuation contrast to make XCT a viable method to distinguish between olivine crystals and their internal melt inclusions [Nakashima et al. 1997; Créon et al. 2018; Richard et al. 2019; Jorgenson et al. 2025].

In total, twelve XCT scans were collected, imaging 147 olivine crystals. The data were collected on a cone-beam Zeiss Versa Xradia 410 X-Ray Microscope hosted at the University of Leeds, School of Civil Engineering. To maximise

the X-ray attenuation contrast between olivine crystals, melt inclusion glass, and vapour bubbles, low X-ray energies were used (50 kV) and a beam power of 7 or 10 W. Exposure times varied between 4 to 10 seconds per projection, depending on the sample, and power binning of two was used. Between 1301 and 1601, projections were collected over 360° without frame averaging. Similar imaging conditions were used for each sample to keep the data as consistent and comparable as possible. For this reason, the same objective lens was also used (4×), producing reconstructed pixel sizes between 3.6–5.7 µm.

The acquired image data were then reconstructed using the proprietary Zeiss software associated with the XCT machine (`Reconstructor`). No beam hardening correction or image calibration was applied. Image data was reconstructed and saved as 32-bit data to avoid loss of image quality and pixel information.

2.3 XCT data and image processing

The data acquired from twelve XCT scans were processed using Thermo Scientific™ `Avizo` © software. A standard image processing workflow was implemented to identify and analyse the different phases of interest, identified by greyscale variation. This is described below and a visual summary provided in Figure 2B).

The image datasets were separated into isolated 'subvolumes', each incorporating an individual crystal for further processing. This was done to accommodate variation in greyscale intensities between crystals, the result of varying scan conditions, sample preparation, and, more importantly, variation in olivine composition (see Figure 3B and 3C). This can be resolved well in XCT data, and has even been partially quantified for rapid petrological characterisation of magmatic olivine compositions in Pankhurst et al. [2014]. Each subvolume, containing a single olivine crystal, was processed separately to ensure effective segmentation and to take into account this variety in greyscale intensity.

A minimal edge-preserving filter was applied to each subvolume to reduce noise within the image data. The Anisotropic Diffusion function was applied with low to minimal thresholding values (1500), using a single iteration to reduce the chance of oversmoothing [Perona and Malik 1990; Schlüter et al. 2014]. Segmentation of the main phases of interest within the filtered data was carried out using the Watershed Thresholding Algorithm [Beucher and Lantuéjoul 1979; Beucher and Meyer 1993; Roerdink and Meijster 2001; Schlüter et al. 2014]. Greyscale ranges for each phase of interest were selected manually from the histogram and refined from visual inspection (Figure 3C and Figure 4). These are used as an input for the Watershed Algorithm, which treats the dataset as a topographical map with highs and lows, where regions with higher gradients are identified as boundaries. These highs and lows are based on the visually determined greyscale ranges, and are progressively 'filled' accordingly from seed regions as the algorithm progresses through the image dataset [Beucher and Meyer 1993]. This algorithm provides more robust computational segmentation than manual segmentation using only visually determined greyscale thresholding. Once complete, the process produces a separate dataset for each segmented phase that can then be analysed and manipulated independently. The subvolumes were thus segmented into four classes: olivine, melt inclusion glass, bubble, and spinel where present (Figure 2B and Figure 3D). These new datasets were then refined, separated and labelled, allowing identification of individual melt inclusions and bubbles, and quantification of their volumes and 3D geometries.

In this study, only fully isolated and complete inclusions were considered to reduce the likelihood of loss of CO_2 from degassing and re-equilibrium with the carrier melt through embayment necks and cracking. To do this, an olivine 'Mask' was created and applied to isolate only phases internal to the olivine crystals. In this way, features such as embayments and cracked inclusions that were in contact with the edges of the crystal were excluded from analysis. To remove unwanted noise, or objects too small to accurately resolve and quantify, the data was further filtered to remove features smaller than three voxels using the 'Remove Small Spots' function. Geometrical and volumetric data for inclusions and bubbles were extracted from the filtered data using the 'Label Analysis' function in `Avizo`. For each processed crystal subvolume, the following parameters were saved for both the melt inclusion and any associated bubbles: volume, long and short dimensions, surface area, aspect ratio, shape, and orientation. Three-dimensional renderings of the crystals and internal phases (melt, bubbles, and spinels) were also generated for visualisation purposes, and to allow for further identification of crystals and inclusions for subsequent targeted geochemical analyses (This workflow is summarised in Figure 2B.)

2.4 Quantifying errors associated with XCT-generated melt inclusion volumes

Melt inclusion and bubble volumes derived from XCT are subject to both systematic and random errors [Lin et al. 2015]. These can be quantified and mitigated, and it is important to consider these to improve the quality and precision of the data produced from this technique.

Random errors are associated with the position of the sample within the scan voxel grid and the effect this has on the positioning of boundaries. This is referred to as the 'partial volume effect', and is a function of the XCT spatial resolution (voxel size), and the size of the object of interest, assuming sufficient contrast between phases has been achieved from scan conditions. The random error associated with volume quantification of an object smaller than 8 voxels has been shown to be larger than the volume of the object itself, with this reducing to around 10 % for any object up to 260 voxels in size [Lin et al. 2015]. For objects larger than this, random errors will have a minimal effect on volume quantification.

To account for random errors within this study, any objects smaller than 3 voxels were discarded completely. Ideally, only inclusions larger than 260 voxels should be analysed to reduce the impact of random errors, however, a compromise between sample size and scan resolution was necessary to enable sufficient data collection. For inclusion volumes, the smallest objects considered were >50 voxels. Vapour bubbles were generally much smaller, and therefore, the random

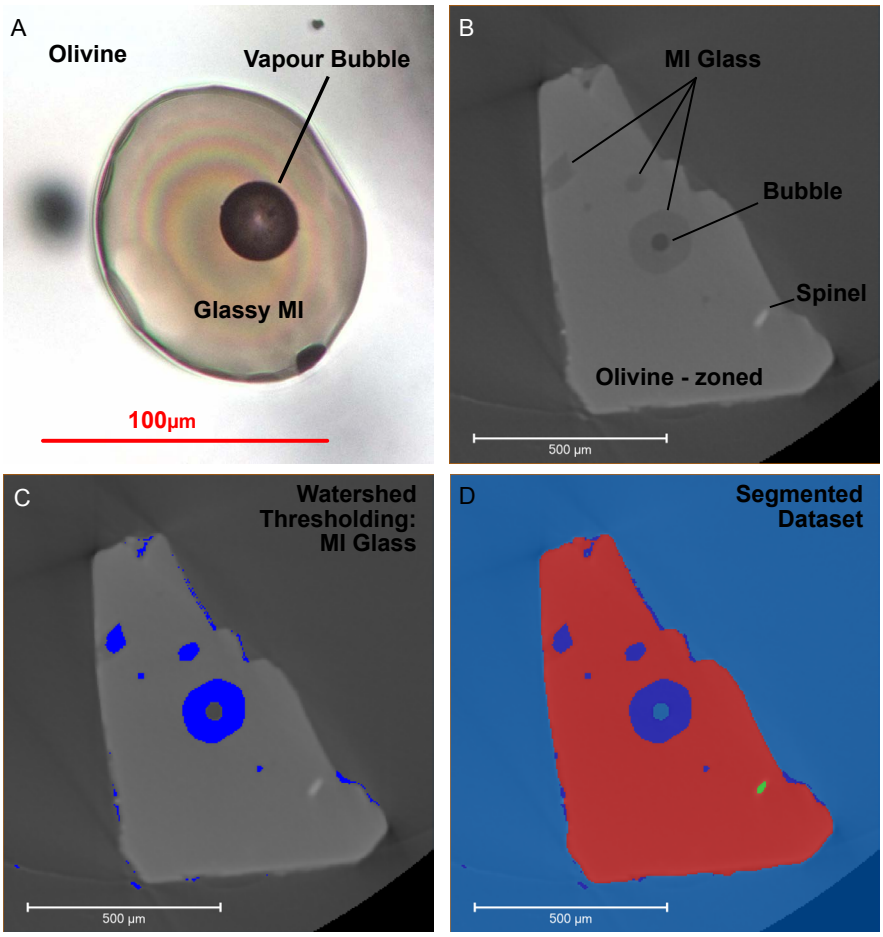

Figure 3: [A] Photomicrograph of a glassy melt inclusion containing a bubble. [B] 2D projection of olivine, melt inclusion and bubble showing variation in greyscale associated with X-ray attenuation contrast. [C] Orthoslice showing visually the process of thresholding and segmentation. Greyscale values associated with melt inclusion glass are selected, and the voxels are highlighted to separate the data into the phases of interest. [D] Segmented dataset (red: olivine, dark blue: melt inclusion glass, pale blue: air and vapour bubble, green: spinel).

errors associated with the bubble volumes attained from this study are non-trivial. Due to the more regular, spherical habit of most bubbles in inclusions, estimating these volumes from optical imagery may likely be sufficient. To investigate this, a subset of melt inclusion bubbles were measured optically and compared to the XCT-generated bubble volumes. These were selected randomly from the original sample set, and span the range of sizes of bubbles in this study.

Systematic errors typically relate to scan conditions and image processing, such as the choice of thresholding algorithm and segmentation greyscale values. These can be quantified and minimised by repeat scans and processing [Lin et al. 2015]. To quantify systematic errors associated with the choice of thresholding values in this study, repeat processing was adopted for melt inclusion glass thresholding. The Watershed Segmentation algorithm was applied three times: 1) ideal thresholding—visual confirmation of the optimum greyscale range for melt inclusion glass, 2) maximum thresholding—the largest feasible greyscale range for inclusion glass, yielding the largest volumes, 3) minimum thresholding—the smallest greyscale range for melt inclusion glass, yielding the lowest reasonable volumes for inclusions (Figure 4). The volumes attained from each of these rounds of processing were compared to give a percentage uncertainty for the melt inclusion volumes.

To allow for consistency and repeatability between subvolumes and scans, the upper and lower bounds for the thresholding values of melt inclusion glass were adjusted as relative percentages of the total greyscale range for each subvolume. Visual confirmation showed that increasing or decreasing the thresholding greyscale range for inclusion glass by ±2 % altered inclusion sizes without incorporating large amounts of internal noise within the crystal (Figure 4). This was problematic for some of the smaller inclusions, particularly where they are in close proximity to crystal edges or each other. Overall, however, this provided a consistent and repeatable method that could be applied to all crystal subvolumes, providing a maximum and minimum volume for melt inclusions and therefore allowing for a rudimentary systematic error quantification. This is likely to be a considerable overestimation of errors, however, our approach provides a consistent workflow that can be applied to each scan and subvolume to categorically constrain melt inclusion volumes within a reasonable range of uncertainty. Another technique that could improve the error quantification further would be the addition of a volume calibration into each sample, such as a tungsten sphere as in Hanyu et al. [2020], however, this was not implemented in this study.

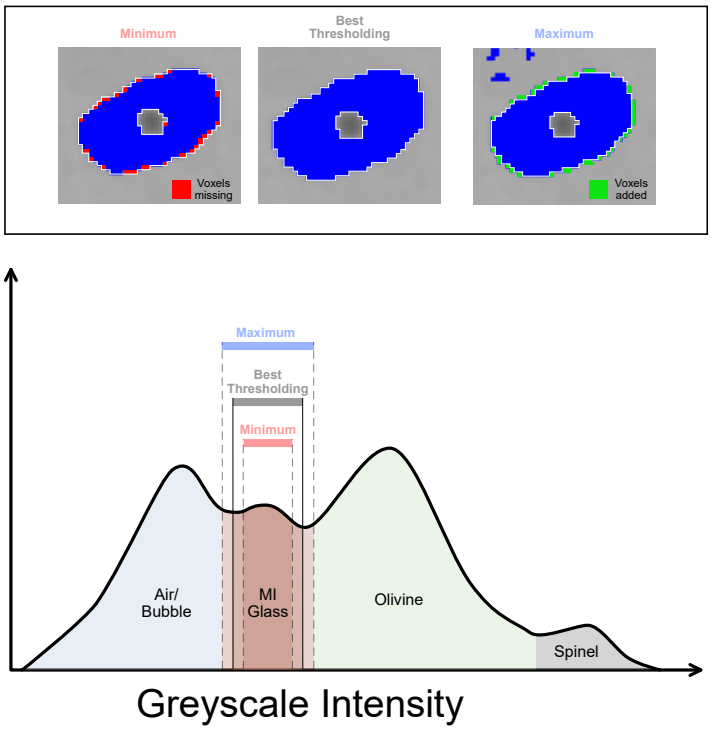

Figure 4: [A] Photomicrograph of a glassy melt inclusion containing a bubble. [B] 2D projection of olivine, melt inclusion and bubble showing variation in greyscale associated with X-ray attenuation contrast. [C] Orthoslice showing visually the process of thresholding and segmentation. Greyscale values associated with melt inclusion glass are selected, and the voxels are highlighted to separate the data into the phases of interest. [D] Segmented dataset (red: olivine, dark blue: melt inclusion glass, pale blue: air and vapour bubble, green: spinel).

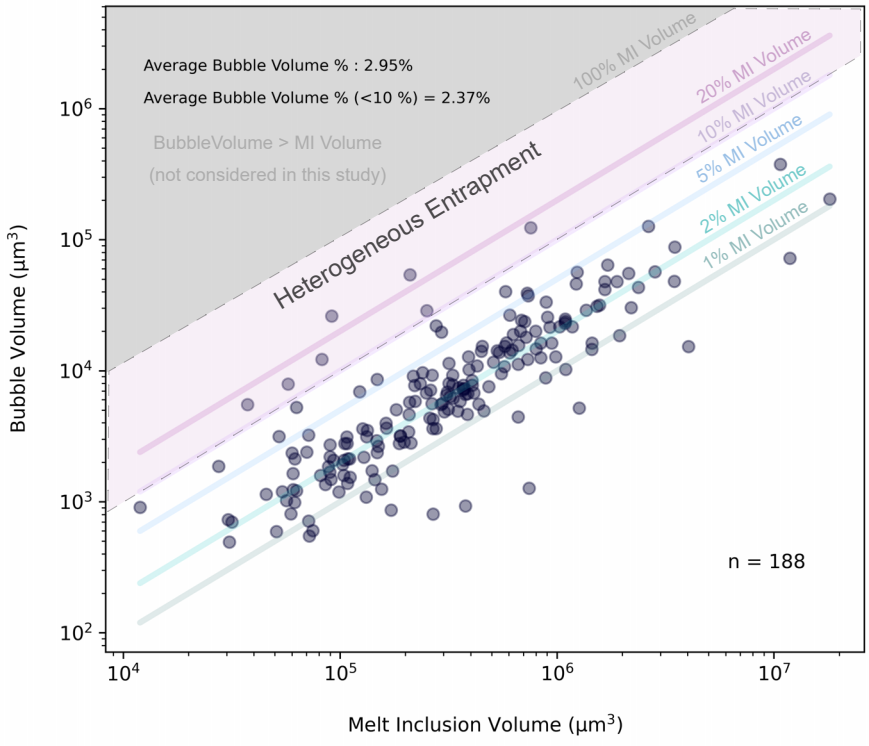

Figure 5: A scatter graph showing bubble volumes against melt inclusion volumes from this study. Bubbles commonly occupy around 2 % of the total inclusion volume, irrespective of the melt inclusion size, however there are many outliers. Bubbles larger than 10 % of the inclusion may indicate the presence of a vapour phase during entrapment [Moore et al. 2015; Aster et al. 2016; Steele-MacInnis et al. 2017].

3 Results

In this study, a total of 92 olivine crystals from 10 different eruption units were successfully imaged and processed. All crystals contained at least one inclusion, with some containing over 15 inclusions large enough to be resolved and quantified with the scan conditions used. In total, 350 inclusions were identified and analysed. Over half of these (194) contained a bubble larger than 3 voxels in size. While, the majority of inclusions contained one singular bubble, a small number hosted two or more. In some scans, there was evidence that some inclusions may have contained multiple bubbles; how-

ever, these were smaller than the 3-voxel threshold required for quantification.

Melt inclusion volumes vary by several orders of magnitude, with the largest around 1.8×10^7 μm^3 (ca. 135,000 voxels) and the smallest inclusion considered in this study around at 7.75×10^3 μm^3 (56 voxels) (Figure 5). Most inclusions were large enough that random errors have little impact on the volumes; however, 27 of the 350 inclusions are below the 260-voxel threshold, which may result in random errors of >10 % for these volumes [Lin et al. 2015].

In contrast, bubble volumes are much less certain and would require a higher scan resolution to accurately quantify. Of the 194 bubbles considered here, 38 are larger than the 260-voxel threshold, above which random volumetric errors are lower than 10 %. The rest are smaller than this and will therefore be strongly impacted by random errors. Six bubbles are smaller than eight voxels, resulting in a volumetric error larger than the bubble itself [Lin et al. 2015] and have been removed from our dataset. The largest bubble recorded in this study is 2.0×10^5 μm^3 (1538 voxels), and the smallest still retained in the dataset is just 438 μm^3 (8 voxels). The majority of bubbles have volumes that are subject to uncertainties >10 % of the bubble volume, however, they have been included in the results of this study for completeness. To improve bubble volumes determined using XCT, smaller sample dimensions and therefore better voxel resolution would be required. Due to the more regular, often spherical, geometry of most bubbles, optical microscopy appears to be a better technique for determining accurate bubble volumes compared to the scan resolution used here. To investigate this, a subset of 29 melt inclusion bubbles were measured optically. Results show that on average, XCT underestimated the bubble volume by almost 20 %, in comparison to using optical measurements and the assumption of a spherical bubble geometry (Figure 6).

Using XCT-derived volumes, bubbles make up an average of 2.95 % of the total inclusion volume, however, this varies widely from 0.2 to 29 %. The size of the inclusion does not appear to have an influence on the bubble volume proportion (Figure 5). A total of seven bubbles have volumes greater than 10 % of the inclusion volume, suggested to indicate heterogeneous trapping of a vapour phase, present in the magmatic system at the time of inclusion formation [Moore et al. 2015; Aster et al. 2016; Steele-MacInnis et al. 2017]. When discounted, this reduces the average bubble volume percentage to 2.37 % of the total inclusion volume.

As described in the methods section, systematic errors associated with thresholding were quantified by repeat analyses, varying segmentation by ±2 % of the total greyscale range within each filtered subvolume. In general, the change in thresholding resulted in an average variation in the inclusion volume of ±25 %. Larger thresholding errors are associated with smaller inclusions, where a thresholding change has a larger effect on the volume, and where the voxel number is lower (Figure 7). There are also cases where greyscale values for different inclusions vary substantially within a single crystal, likely due to different inclusion compositions. Where possible, repeat processing was carried out to optimise the thresholding for each of the main inclusions. While these errors may appear fairly large, it is important to note that other conventional techniques, such as optical microscopy, cannot directly quantify volumetric errors due to the combination of uncertainty in intersection angle, simplification of geometry and depth assumptions.

4 Discussion

4.1 Comparison with 2D melt inclusion volume estimates

Melt inclusion volumes are typically derived from measurements taken using optical microscopy and the assumption of an ellipsoidal geometry. The long and short axes of an ellipsoid are measured from a 'best fit' ellipse drawn around the imaged inclusion (as shown in Figure 1) [Tucker et al. 2019; Mironov et al. 2020; DeVitre et al. 2023; Van Gerve et al. 2024]. Using these long and short dimensions (a and b), a third, vertical (depth) dimension (c) is assumed, and used to calculate the theoretical volume of an idealised inclusion [Tucker et al. 2019; Hanyu et al. 2020; Wieser et al. 2021; Van Gerve et al. 2024]. The most common assumptions used to calculate this third dimension are:

1. c is the arithmetic mean of the measured dimensions (a and b) [Moore et al. 2015; Tucker et al. 2019; Wieser et al. 2021; Van Gerve et al. 2024]:

$$c = \frac{a+b}{2}. \tag{2}$$

2. c is equal to the shortest axis (b) (spheroidal geometry) [Hartley et al. 2014; Neave et al. 2014; Tucker et al. 2019; Hanyu et al. 2020; Van Gerve et al. 2024]:

$$c = b. \tag{3}$$

3. c is equal to the geometric mean of the two measured dimensions [Ni et al. 2017; Tucker et al. 2019]:

$$c = \sqrt{ab}. \tag{4}$$

To explore which of these is likely to provide the best approximation of inclusion geometry, and therefore volume, Tucker et al. [2019] performed simulations of randomly oriented inclusions with a triaxial ellipsoidal geometry ($a \neq b \neq c$) sliced by a planar surface. Their results show that determining the third dimension can be extremely problematic. They ultimately favoured using the arithmetic mean, partly due to its relatively symmetric, Gaussian-like error distribution. The estimated uncertainties in the resultant volume were considerable, around ±40 %. This approach has since been adopted in several studies for estimating inclusion volumes [e.g. Wieser et al. 2021; Van Gerve et al. 2024]; however, it is important to note that in their simulations, the intersection plane always cuts the inclusion through the centre. In reality, this may not occur, and it is also possible that the inclusion geometry may not reflect a triaxial ellipsoid, making these errors likely to be a minimum at best. DeVitre et al. [2023] and Mironov et al. [2020] show that volume errors can be reduced if a depth dimension is measured, rather than assumed, using a microscope with a

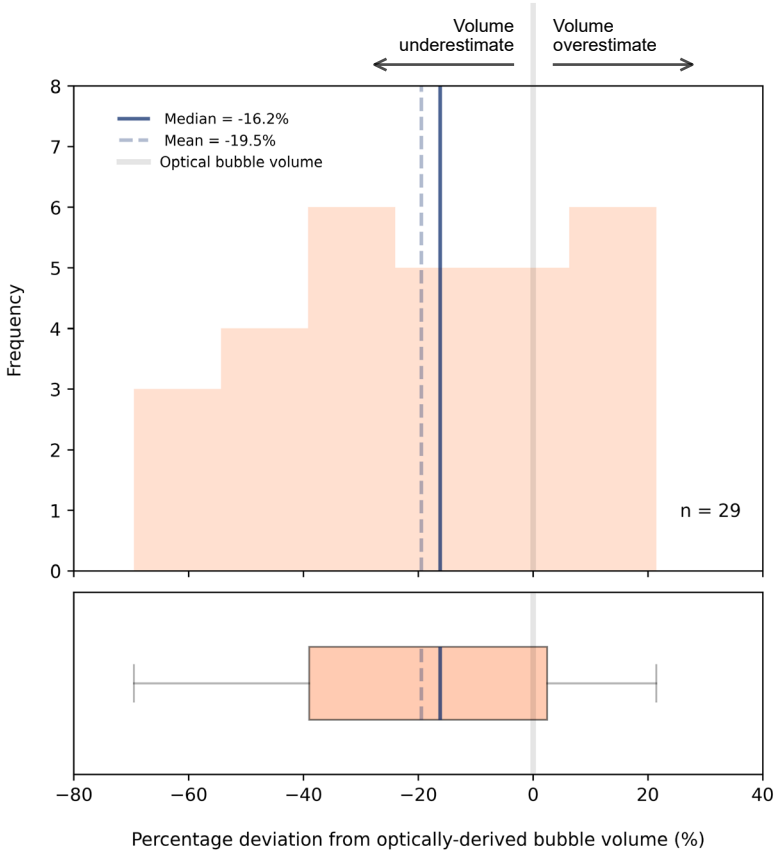

Figure 6: A subset of melt inclusion bubbles were measured optically to compare against XCT-generated bubble volumes. The histogram shows the percentage deviation of XCT-derived bubble volumes from optically derived and measured bubble volumes, assuming the geometry of a sphere. This shows the limitation of using XCT for bubble volumes at the spatial resolution of this study, as most XCT volumes are underestimating the bubble volumes by an average of around 15–20 % in comparison to the optically-derived volumes. These are taken to be the more accurate volume due to the sphericity of the bubbles and the limitations associated with the spatial resolution of the XCT scans. The optical images for each bubble are provided in the Supplementary Material 1 (Figure S4).

calibrated focus. Additionally, it is possible to rotate polished samples by 90° and re-polish to provide a clearer view of the third dimension of an inclusion. This is a destructive process that requires a considerable amount of time and crystal manipulation; however, for 'regular' inclusion geometries it can reduce volume errors to <20 % [Mironov et al. 2020; DeVitre et al. 2023].

To compare XCT-derived volumes with those estimated using the above 2D methods, we calculated volumes for each inclusion in this study using the assumption of an ellipsoidal shape. We extracted the long (a) and short (b) axes of inclusions from XCT data. The c axis was calculated using the three assumptions listed above (Equation 2, Equation 3, and Equation 4). It is important to note that XCT-derived dimensions are the true longest and shortest axes of the inclusions, and are not affected by inclusion and intersection plane orientation, as would typically be the case if imaged optically. Therefore, these represent a best-case scenario for 2D-based volume estimates. The results of this comparison, shown in Figure 8, demonstrate that for most inclusions, 2D methods overestimate inclusion volume by around 13–40 %, but sometimes much more.

For the samples studied here, inclusion geometry appears to conform more closely to that of a spheroid ($a > b \approx c$) than a triaxial ellipsoid ($a \neq b \neq c$) (Figure 8). Volume estimates generated using this assumption (Equation 3), are notably closer to XCT-generated volumes than those using the other assumptions, with an overall deviation of <14 %. In comparison, volumes generated using a depth dimension calculated from Equation 2 and Equation 4, are, on average, almost 40 % larger than XCT-generated volumes; however, in the most extreme cases, this can extend to >200 %. These extreme cases generally occur for melt inclusions that have higher aspect ratios (Figure 9). Of the 350 inclusions scanned, most have an aspect ratio between 1 and 2. Volumes calculated for inclusions with more elongate geometries deviate substantially from XCT-derived volumes, particularly when using dimensions generated from Equation 2 and Equation 4. Again, assuming a spheroidal geometry appears to more accurately recreate XCT-generated inclusion volumes, particularly at these more extreme geometries.

Our results suggest that conventional methods may be regularly overestimating inclusion volumes, possibly by larger values than those determined by Tucker et al. [2019]. For the inclusions we analysed, the assumption of a spheroidal, rather than triaxial ellipsoid geometry, would provide a better representation of inclusion shape, and would generally produce more robust volume estimates from 2D measurements. Whilst the most accurate method, this can still overestimate inclusion volumes by up to 50 %. Furthermore, the comparisons shown in Figure 8 and Figure 9 do not take into account the variation in measured dimensions resulting from the in-

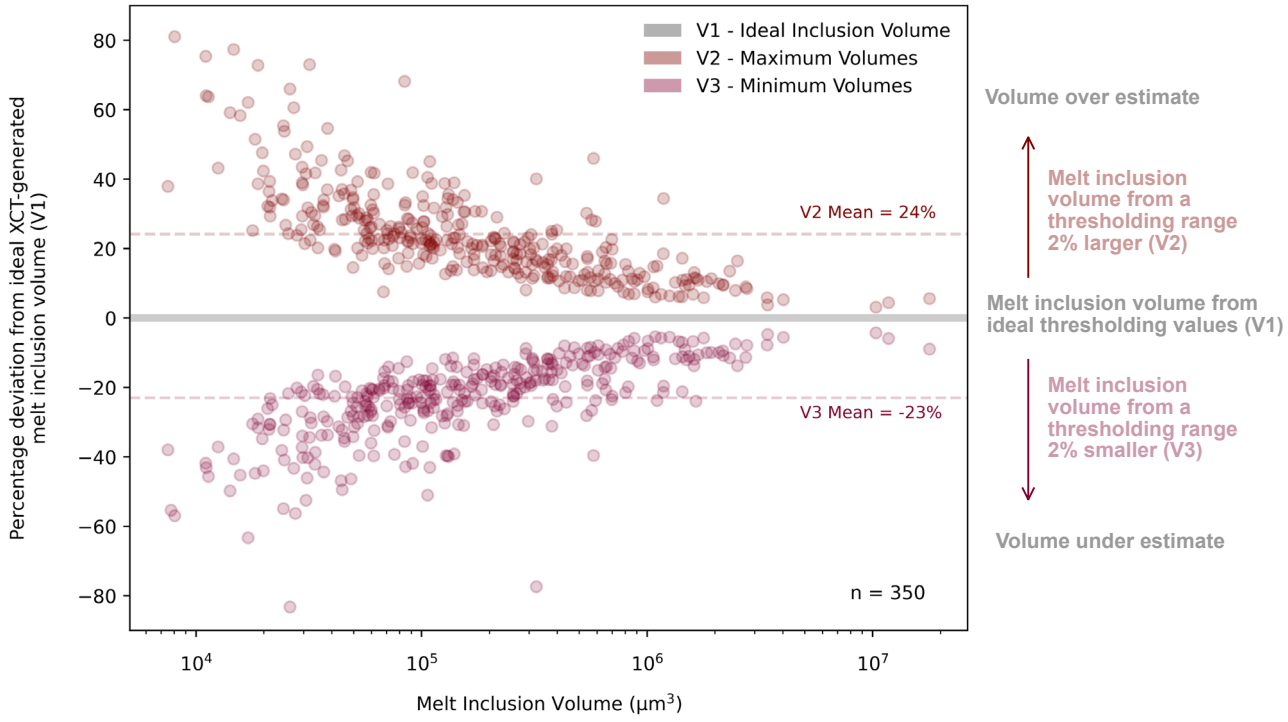

Figure 7: A scatter graph showing systematic error quantification for XCT-derived melt inclusion volumes. Changing thresholding values by ±2 % of the total greyscale range for each subvolume results in an average variation of around ±25 % for melt inclusion volumes. This is lower for larger inclusions and higher for smaller inclusions.

clusion intersection angle, introduced during polishing. The percentage deviation from XCT-generated inclusion volumes in this study is therefore a best-case scenario, with actual 2D volume estimates likely to be considerably more uncertain.

For 'regular' inclusion geometries, it is possible to improve optical volume determinations by taking additional steps, such as using a calibrated microscope and double polishing crystals at right angles to directly measure, rather than infer, the third depth dimension. Using such techniques DeVitre et al. [2023] were able to recreate XCT-generated melt inclusion volumes to within ~10–20 %, however, they note that for inclined inclusions and more 'irregular' geometries, such as those with extreme aspect ratios, the results will be less accurate. Therefore, while it is possible to improve optical volume estimates, at least for some inclusions, preparing large sample sets for such analysis would be very time-consuming. If available, XCT analysis would therefore be both preferable and more accurate. Furthermore, using XCT analysis avoids additional complications that may reduce the accuracy of optically derived volumes, such as inclusion faceting or the presence of additional mineral phases (e.g. spinel) within the inclusion. If collected at a sufficient resolution, XCT data can accurately constrain complex inclusion geometries, and the thresholding of the data removes any internal mineral phases from the array of voxels used to calculate volumes.

4.2 Melt inclusion volume error and CO_2 reconstructions

To explore how inclusion volume errors can affect reconstructed CO_2 concentrations, we generated a simulated geochemical dataset to test inclusion volumes generated from the conventional, 2D methods in this study against the true inclusion volumes generated from XCT analysis. Random numbers were generated within a reasonable range for the parameters required to reconstruct CO_2 in an inclusion bubble from Raman Spectroscopy analysis (Equation 1). These values were derived from a combination of recent melt inclusion studies that have successfully applied Raman Spectroscopy to determine total melt inclusion CO_2 contents. These include a range of samples from a variety of geological and tectonic settings to encompass the likely range of all parameters within reasonable limits [Hanyu et al. 2020; Wieser et al. 2021; Feignon et al. 2022; Van Gerve et al. 2024].

Numbers were randomly generated from a uniform distribution for CO_2 densities in the vapour bubble between 0.05 and 0.5 $g^{-1}\,cm^3$ [Hanyu et al. 2020; Feignon et al. 2022; Van Gerve et al. 2024]. These were assigned at random to the inclusions containing a bubble, as it has been suggested that there is no correlation between inclusion or bubble size and CO_2 density [Hanyu et al. 2020]. Similarly, melt densities between 0.26 and 0.28 $g^{-1}\,cm^3$ were used to reflect minor differences within a generally basaltic melt composition, as this is the most likely composition of melt to be trapped during olivine formation [Stolper and Walker 1980]. For bubble volumes, the XCT value was used throughout. Using these simulated pa-

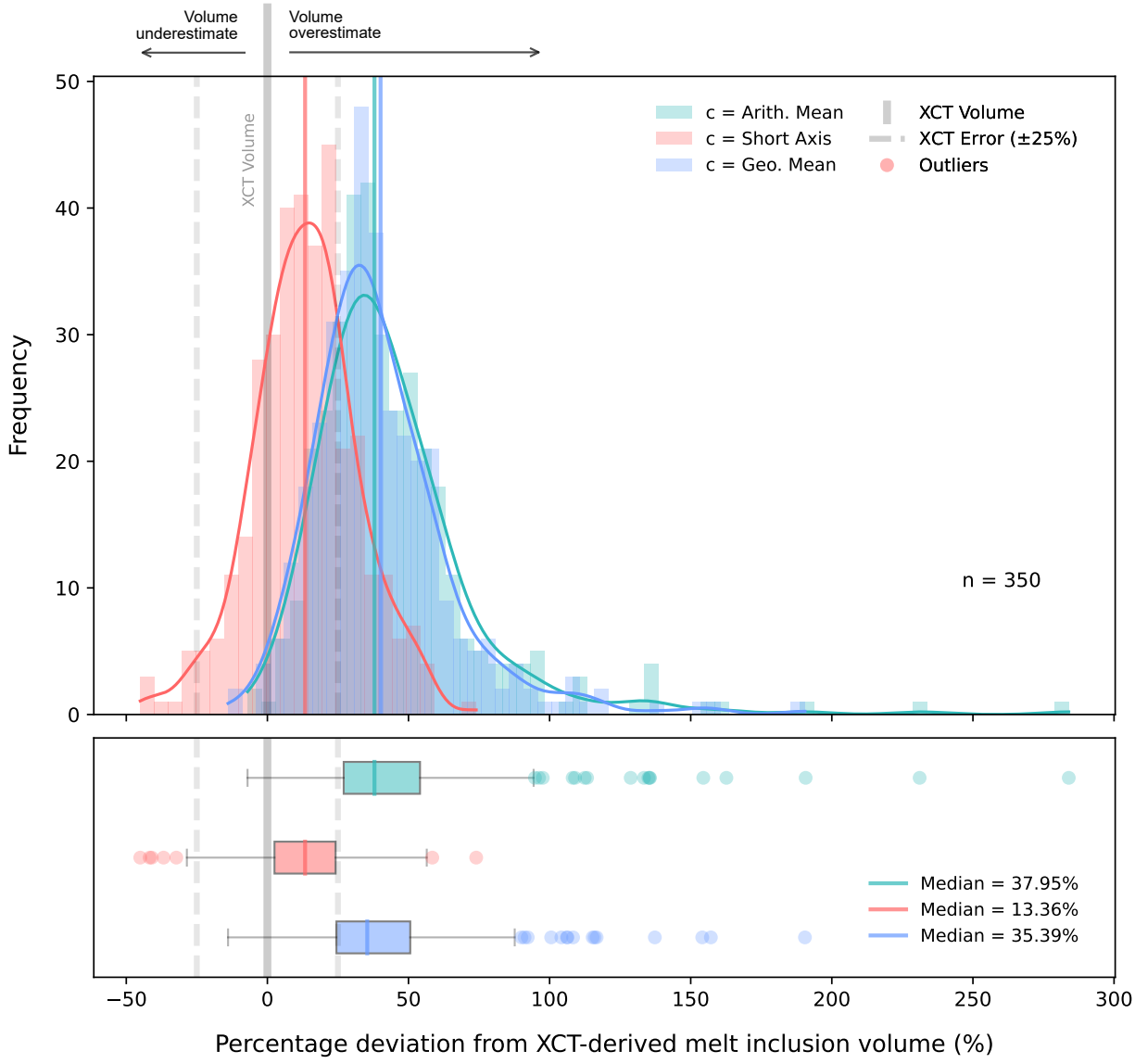

Figure 8: Histogram and boxplot showing the distribution in melt inclusion volumes generated from the three main 2D methods compared to XCT-generated melt inclusion volumes.In general, all assumptions resulted in an overall overestimate of inclusion volume. Using the shortest axis as the depth dimension resulted in the best volume estimates, only overestimating volumes by around 14 % in comparison to XCT-derived values. Medians used due to the skewed distribution.

rameters, changing only the inclusion volume, a bubble CO_2 concentration was calculated for each technique (using Equation 1).

The results of this simulation, shown in Figure 10, demonstrate how the errors in inclusion volumes arising from two-dimensional measurements can result in substantial underestimations of bubble CO_2 concentrations. Bubbles, where present, can contain >90 % of the overall inclusion CO_2, and therefore this can have a considerable impact on total magmatic CO_2 estimates [Moore et al. 2015]. Overall, inclusion volume was consistently overestimated by the various two-dimensional methods applied in this study, resulting in underestimation of bubble CO_2 concentration in comparison to those calculated from XCT-derived inclusion volumes. For example, an average overestimation of around 50 % in inclusion volume results in a ~30 % underestimate in bubble CO_2 concentration. Although less common, underestimates in inclusion volumes have a much larger impact on bubble CO_2 reconstruction, due to the effect this has on the ratio between bubble and inclusion volume. A 20 % underestimate in melt inclusion volume results in ~35 % overestimate in bubble CO_2. The only 2D method that consistently underestimated inclusion volume in this study was the most conservative approach, assuming that the inclusion depth is equal to the shortest measured axis (Equation 3—spheroidal inclusion geometry). This method underestimated the volume of ~20 % of the inclusions in this study (75 of 350 inclusions). In general, however, despite the tendency to underestimate volumes, this method almost always provides the closest approximation to actual inclusion volumes. This must therefore be considered if using

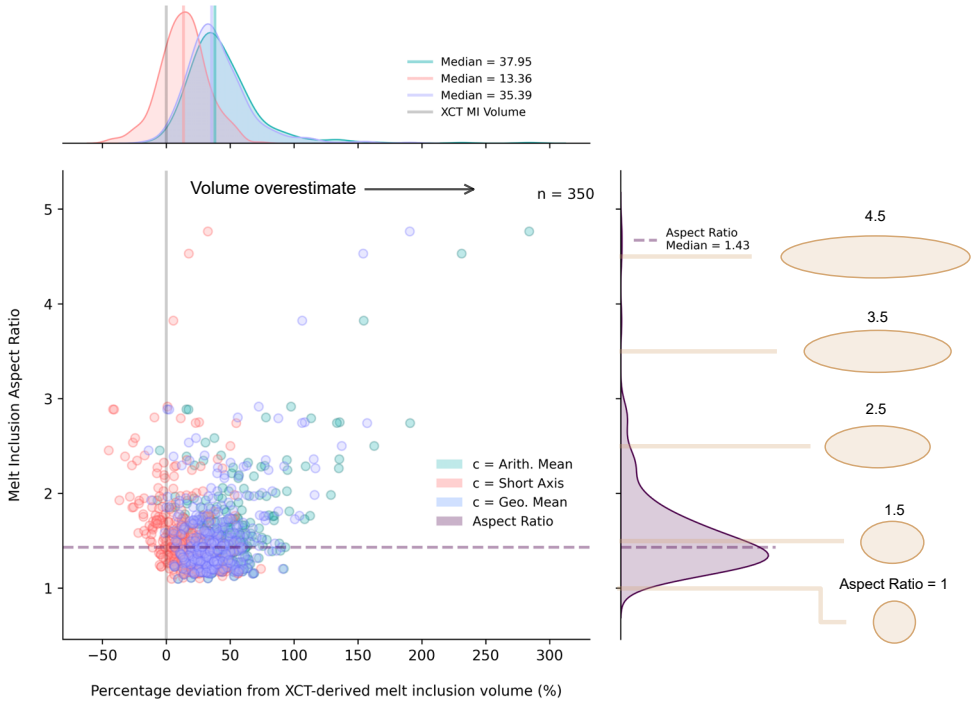

Figure 9: Scatter graph showing the deviation from XCT-derived melt inclusion volumes compared with inclusion aspect ratio. More extreme aspect ratios generally result in larger errors for inclusion volume; however, using the shortest axis as a depth dimension appears to be the most robust representation for melt inclusion geometry and generally produces melt inclusion volumes close to XCT-derived volumes.

Table 1: Parameters used to generate bubble CO_2 concentrations using Equation 1

Parameter	Values
$\rho_{CO_2 bubble}$	0.05–0.5 $g^{-1}\,cm^3$
V_{bubble}	XCT Bubble Volume
ρ_{melt}	2.6–2.8 $g^{-1}\,cm^3$
V_{melt}	XCT-generated and 2D methods inclusion volume

optical measurements and assumptions to determine inclusion volumes for CO_2 reconstructions, as there are competing factors affecting the suitability of the various methods.

When considering the systematic errors in inclusion volumes generated from XCT, an average deviation of ±25 % in inclusion volume results in bubble CO_2 estimates that deviate by −20 to 30 % for over- and under-estimation of inclusion volumes, respectively. We can consider these to be a maximum uncertainty range in inclusion volume and respective reconstructed bubble CO_2 concentrations. XCT allows for this quantification of uncertainty in inclusion volume estimates that can not be derived from two-dimensional, optical inclusion measurements alone. This therefore allows for the propagation of error and uncertainty through the reconstruction of bubble CO_2 concentration, resulting in better quality of data from melt inclusion analyses.

These large differences in bubble CO_2 concentrations, the result of varying and uncertain melt inclusion volumes, can lead to important geological implications. For example, CO_2 saturation pressures are commonly used for inclusion barometry to determine magma storage depths [Anderson 1976; Wieser et al. 2021]. This was investigated using a theoretical inclusion containing 1000 ppm of CO_2 with an uncertainty of just ±25 %, introduced from melt inclusion volume quantification errors equivalent to ~50 % overestimate to ~20 % underestimate in inclusion volume. These errors result in CO_2 saturation pressure differences of around ±50 MPa (calculated using `VolatileCalc` [Newman and Lowenstern 2002]; calculation parameters included in Table 2). This equates to uncertainties in magma storage depths of ±~2km (for magma storage in a typical basaltic crust: density: 2.7 $g^{-1}\,cm^3$). This is comparable to similar calculations conducted by DeVitre et al. [2023]. They found that assumption-based inclusion volumes can result in large and unpredictable errors of a similar magnitude to this study, with inconsistencies of ±~100 MPa at crustal pressures equivalent to ~12km entrapment depth for double-polished crystals, increasing to ±~300 MPa for assumption-based inclusion volumes. The scatter and effect that this has on saturation pressures can evidently be important for geological interpretation, such as understanding the architecture of magmatic systems and processes within the crust, and it is therefore essential that these errors are sufficiently quantified to improve this. XCT provides a method that both improves the accuracy of melt inclusion volumes and therefore subsequent CO_2 concentrations, and allows for uncertainty quantification that can be incorporated into further investigation and analyses.

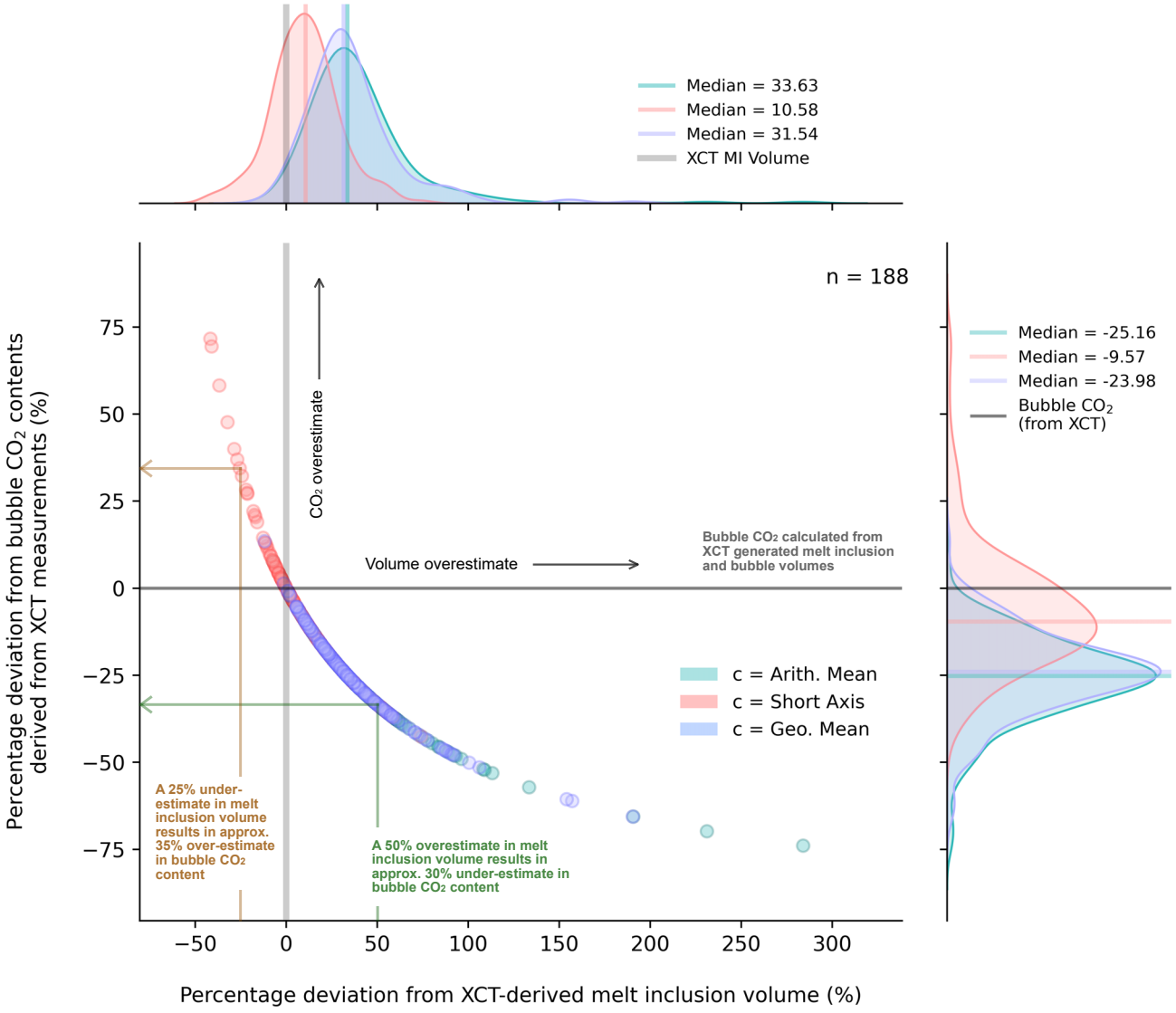

Figure 10: Scatter plot illustrating the effect of over- or underestimation of melt inclusion volume on calculated vapour bubble CO_2 concentrations (Equation 1). The impact of melt inclusion volume estimation using three 2D methods is compared to volumes measured using XCT. Underestimating the melt inclusion volume leads to overestimation of CO_2 contents. The most conservative 2D volume approach, using the short axis as the third unmeasured dimension, leads to substantial overestimates of vapour bubble CO_2. In contrast, less conservative approaches lead to slightly smaller underestimations in vapour bubble CO_2.

Table 2: Parameters used in `VolatileCalc` Saturation Pressure Calculations

Parameter	Values
Melt Inclusion wt. % SiO_2	Typical basaltic melt (49.0 wt. % SiO_2*)
Melt Inclusion wt. % H_2O	Typical arc water content (4.0 wt. % H_2O†)
Temperature (°C)	Typical basaltic melt (1250°C ‡)
CO_2 Concentration (ppm)	1000 ppm (±25 %)

*Stolper and Walker [1980]; †Plank et al. [2013]; ‡Mourey and Shea [2019].

4.3 Melt inclusion populations and characteristics

Another valuable aspect of the application of XCT for melt inclusion studies is the ability to analyse all inclusions within a crystal. This allows for a better understanding of inclusion population characteristics, such as the number of inclusions within a crystal, overall size distributions, common shape characteristics (faceted, elongated, crystallised etc.), spatial location within a crystal, and bubble volume proportion. It is also possible to analyse large inclusion datasets relatively rapidly, without extensive sample preparation [Jorgenson et

al. 2025]. Differences in inclusion characteristics may relate to differences in magma storage conditions and system dynamics, along with volatile content, composition and eruption dynamics [Jorgenson et al. 2025]. Different eruption units were sampled in this study to investigate the magma dynamics at Mocho-Choshuenco Volcano. Differences in melt inclusion population characteristics are identifiable between the eruption units sampled. We discuss some of these features briefly in the sections below.

4.3.1 *Bubble volume proportions between different eruption units*

Bubble formation and entrapment can be affected by a range of factors. It has been suggested that bubble size does not correlate with CO_2 density [Hanyu et al. 2020], however, systematic differences between eruptions may indicate variation in post-entrapment modification processes (PEM), inclusion entrapment history and magma ascent [Moore et al. 2015; Rasmussen et al. 2020; Jorgenson et al. 2025]. The bubble volume proportion can also provide an insight into features such as heterogeneous entrapment, indicating the presence of a fluid/vapour phase, coeval with olivine growth and inclusion entrapment [Steele-MacInnis et al. 2017].

In this study, bubble volume proportion varied between melt inclusions and also between eruption units. On average, bubbles made up 2.95 % of total inclusion volume, however, this reduces to 2.37 % when bubbles larger than 10 % are discounted (Figure 5). This is generally quite low in comparison to studies such as Hanyu et al. [2020] and [Van Gerve et al. 2024]. Of the 188 segmented bubbles, 7 had a volume proportion of >10 %, indicating the possibility of heterogeneous entrapment [Steele-MacInnis et al. 2017]. These inclusions were spread across five different eruption units, indicating that this may be a common occurrence within the magmatic system at the volcano studied (Figure 11).

Average bubble volume varies slightly between eruption units, with some containing what appear to be proportionally smaller bubbles compared to the melt inclusion volumes. The distribution of bubble volume proportions is also distinctive between eruptions (Figure 11). Sampled units: MC5 (Pirehueico), MC21 (Pilmaiquen), MC23 (Arauco), CC (Chanchan cones), and FN (Fui Norte Cones), contain bubbles larger than 10 % of total inclusion volume, however three of these eruptions also contain some bubbles with volume proportions around 7–10 %. This may suggest the presence of a vapour or fluid phase during inclusion entrapment, resulting in larger bubbles [Moore et al. 2015; Aster et al. 2016; Steele-MacInnis et al. 2017; Jorgenson et al. 2025]. In contrast, eruptions MC10 (Grupo Fui cones) and MC15 (Enco) have a very small range in bubble volume proportions, with all falling between 1 and 3 %. These trends may indicate differences in the CO_2 contents, conditions at the time of entrapment and/or different PEM processes. These will be investigated further by more targeted geochemical techniques.

4.3.2 *Melt inclusion alignment*

The spatial arrangement and morphology of melt inclusions can indicate characteristics of different entrapment mechanisms [Roedder 1979; Audétat and Lowenstern 2014; Cannatelli et al. 2016; Wallace et al. 2021]. In this study, the majority of melt inclusions appear to be randomly oriented within the crystal, with little to no relationship between the host crystal shape and inclusion position or orientation. The crystal shape was often irregular due to a combination of external glass and the bias towards broken crystals (necessary to confirm the presence of inclusions when picking prior to scanning). A small number of well-faceted crystals were present, along with a handful number of agglomerates where multiple crystals could be identified, sometimes showing well-faceted crystal edges.

Faceted inclusions are generally interpreted to form from diffusional processes that act to reduce surface free energy, and can indicate long timescales of crystal storage at near-magmatic temperatures [Pamukcu et al. 2015; Wallace et al. 2021]. XCT has been used to quantify the degree of faceting for melt inclusions in quartz crystals [Pamukcu et al. 2013; Pamukcu et al. 2015], along with categorisation of inclusion shapes and morphologies in pyroxene-hosted inclusions [Jorgenson et al. 2025]. Melt inclusion faceting was rarely identifiable in the crystals analysed in this study, and was therefore not investigated further.

In a small number of the crystals analysed in this study, there was evidence of internal alignment of melt inclusions (Figure 12A). When plotted stereographically, the long axes of the inclusions cluster, indicating a common orientation within the crystal. This direction varies between crystals due to the random orientation of crystals within the XCT scan space, however, the clustering suggests that within a single crystal there is a common alignment of inclusions (Figure 12A). Due to the irregular shape of most crystals, relating this alignment to crystal habit and host crystallographic orientation was not possible. The alignment may suggest a common mechanism for inclusion entrapment, such as anisotropic crystal development during periods of rapid skeletal growth as the result of undercooling [Mourey and Shea 2019]. Alternatively, inclusion alignment could reflect post-entrapment maturation of melt inclusion shapes, such as faceting [Pamukcu et al. 2015]. This will require further investigation to determine the host crystal orientation and the relationship to inlusion alignment direction.

Similar alignment, along with internal complexities, was also identified in some crystals with embayments. Embayments can reflect resorption textures, indicating disequilibrium conditions between the olivine and melt body [Laumonier et al. 2019]. Alternatively, they can also occupy areas where complete entrapment of a melt inclusion has not proceeded due to insufficient crystal growth. They can therefore reflect both primary and secondary melt inclusion processes. Crystals such as CC-A (pictured in Figure 12B) exhibit a combination of isolated central melt inclusions and embayments that all appear to align with each other. Crystal MC1-D also exhibits a strong alignment of a complex embayment feature running through the centre of the crystal. This is predominantly filled with a vapour phase, with small amounts of internal melt (now silicate glass) present in the XCT image data forming a complex geometry (Figure 12C). The association of both inclusions and embayments indicate

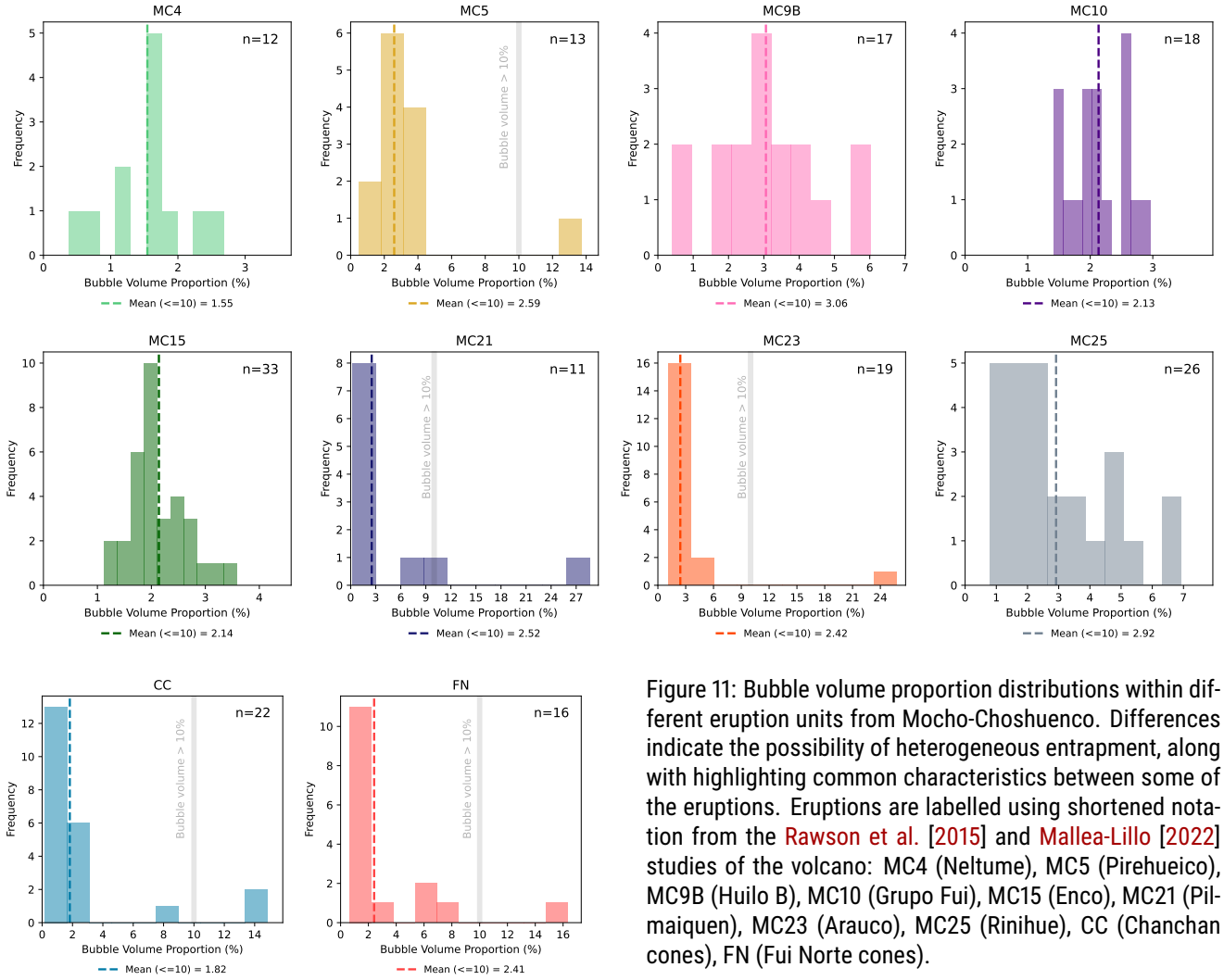

Figure 11: Bubble volume proportion distributions within different eruption units from Mocho-Choshuenco. Differences indicate the possibility of heterogeneous entrapment, along with highlighting common characteristics between some of the eruptions. Eruptions are labelled using shortened notation from the Rawson et al. [2015] and Mallea-Lillo [2022] studies of the volcano: MC4 (Neltume), MC5 (Pirehueico), MC9B (Huilo B), MC10 (Grupo Fui), MC15 (Enco), MC21 (Pilmaiquen), MC23 (Arauco), MC25 (Rinihue), CC (Chanchan cones), FN (Fui Norte cones).

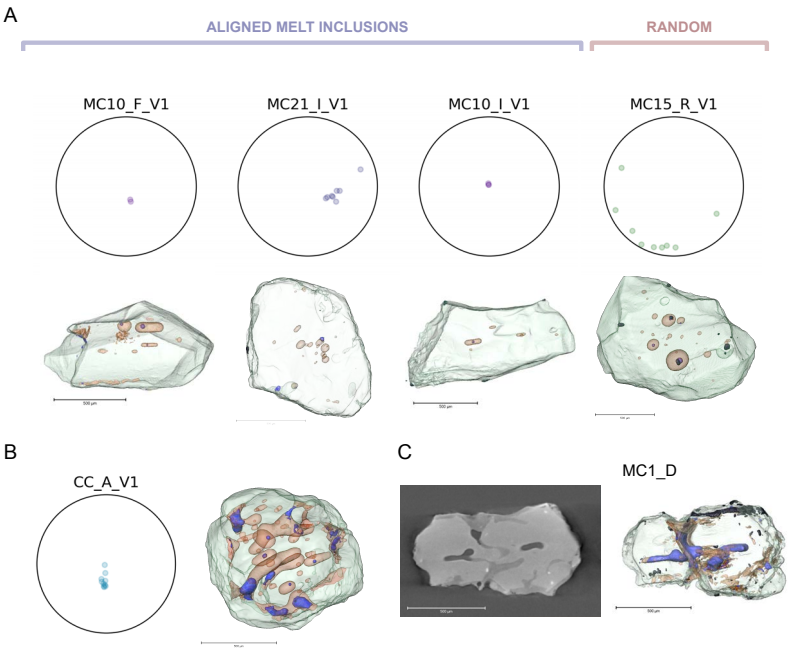

Figure 12: [A] 3D renderings of olivine crystals and melt inclusions from XCT data, showing systematic alignment of melt inclusions. Stereographic plots showing the orientation of the long axis of the melt inclusions confirm clustering around a common direction within each crystal. A randomly oriented population of inclusions is also included for comparison. [B] 3D rendering of crystal CC-A showing aligned melt inclusions and embayments. The stereographic plot shows the clustering of the long axis of the inclusions within the crystal, again suggesting a preferred alignment of these features. [C] 3D rendering of crystal MC1-D and a representative projection showing the internal structure. The crystal shows alignment of melt embayments in the centre of the crystal that are predominantly occupied with a vapour phase rather than typical melt inclusion glass.

that the crystals in this study may have undergone complex growth and/or resorption phases, highlighting the importance of three-dimensional imaging and the consideration of population characteristics and geometries. Non-destructive, three-dimensional imaging techniques such as XCT are therefore essential for understanding these processes in more detail. This is necessary to ensure that the geochemical information obtained from melt inclusions, such as CO_2 content, is supported by the correct geological context (i.e. primary or secondary melt inclusions, resorption or growth features).

5 Conclusions

In this study, we apply X-ray Computed Tomography to image a large set of melt inclusion-bearing olivine crystals. The volumetric measurements for inclusions acquired using this technique greatly improve on conventional methods that are currently used for the majority of melt inclusion studies. This improvement is particularly important for the determination of magmatic volatiles such as CO_2 from melt inclusion data. Current studies use melt inclusion volumes that are determined by a combination of measurement, assumptions, and simplification of geometry. The errors and uncertainties associated with these methods are likely to be substantial (>40 % of the total inclusion volume). However, they cannot be definitively quantified. Techniques such as XCT can greatly improve inclusion volume determinations, thus also improving our understanding of magmatic volatiles. In addition, XCT has allowed the observation of the three-dimensional configuration of melt inclusion populations, allowing identification of features such as inclusion alignment and variable characteristics such as shape and size. These observations are essential for the understanding of inclusion entrapment, and therefore the context for geochemical data such as volatile reconstructions.

Inconsistencies in melt inclusion volume estimation from 2D measurements can have a considerable impact on reconstructed bubble CO_2 contents (Figure 10). Commonly, 2D methods overestimate inclusion volumes, resulting in an underestimate in subsequent CO_2 concentration within the bubble from methods such as Raman Spectroscopy. We show that an average overestimation of inclusion volume of just 40 % can result in an underestimation of ~25 % for bubble CO_2 reconstruction. This can equate to around ±50 MPa uncertainty in CO_2 saturation pressures, translating to differences in magma storage depth estimates of ±2 km which may greatly affect many geological interpretations for magmatic processes such as crystal growth, inclusion entrapment and magma system architecture. Importantly, these inconsistencies can also substantially affect volcanic hazard interpretations, with uncertainties in calculated magma storage depths affecting the utility of volcanic models developed for seismic and satellite monitoring systems. These uncertainties in volume measurements cannot be quantified using 2D methods alone, and therefore CO_2 concentrations determined from bubble-bearing melt inclusion analyses using techniques such as Raman Spectroscopy are fundamentally limited in their accuracy.

XCT provides a solution for this, allowing for 3D quantification of true melt inclusion geometries. While elegant, it is important to consider the limitations of this technique and to include steps to allow for error mitigation and quantification of uncertainty. This paper details a workflow that can be adapted and applied to large sample suites of melt inclusions, allowing for relatively rapid acquisition and processing of melt inclusion data from XCT image data. We also highlight limitations with the technique, such as the necessity for a compromise between sample size and spatial resolution. This must be considered when determining the quality of the data that is extracted from this technique. For example, we show that at the scan resolutions used in this study, most bubbles analysed will have a volume error of greater than 10 % of the bubble volume. We also show that on average, our XCT thresholding resulted in an underestimate in bubble volume of 20 %, and therefore it may be necessary to continue using optical methods for bubble volume quantification. We also provide a framework for the quantification of volume uncertainty that can be built into the image processing workflow. This results in an average uncertainty of ±25 % for melt inclusion volumes. However, this is proportional to the size of the inclusion measured, with larger inclusions having much smaller volume uncertainties. The definition of this uncertainty is essential for ensuring good data quality and for the incorporation of this into further melt inclusion analyses, to allow for credible geological interpretation of the data.

Similarly, it is important to consider the context of the melt inclusions studied. XCT allows for three-dimensional investigation of melt inclusions and populations within an entire crystal, prior to any removal of material during polishing and inclusion exposure. This can show features such as inclusion alignment and population characteristics that may otherwise be missed. This may allow for a better understanding of inclusion formation mechanisms and, therefore, better application of inclusions for the study of magmatic systems.

Author Contributions

HT contributed to the development and conceptualisation of this study, along with sample collection and preparation, data collection, acquisition and processing, development of methodology, data visualisation and the preparation and writing of this work. DF contributed to the conceptualisation of this study, supervision of the project, funding acquisition, along with reviewing and editing of this paper. AM contributed to the development of the methodology, investigation and data curation in this study, in particular, collecting the XCT data and providing supervision and support with data processing, visualisation and reviewing this work. FB contributed to sample collection and preparation, data processing and visualisation, and provided support in writing and reviewing this work. EM provided support with sample collection and organisation of access to the field site, along with support in reviewing this work. JH provided supervision of this project and reviewed the writing.

Acknowledgements

HT is funded by the National Environmental Research Council (NERC) as part of the Panorama Doctoral Training Partnership (DTP) NE/S007458/1. EM also wishes to thank the FONDECYT Iniciacion project (number 11230197). FB is funded by a UK Science and Technology Facilities Council (STFC) grant ST/V000675/1. Micro-XCT data were acquired in the Centre for Infrastructure Materials, University of Leeds, UK, a UKCRIC Research Facility (EP/P017169/1). We would like to thank the Huilo-Huilo Biological Reserve and Reserva Nacional Mocho-Choshuenco for allowing access to the slopes of Mocho-Choshuenco and the collection of samples.

Data Availability

Data are provided in the Supplementary Material 2 spreadsheet. Raw XCT data files are available from the author upon request.

References

Allison, C. M., K. Roggensack, and A. B. Clarke (2021). "Highly explosive basaltic eruptions driven by CO2 exsolution". *Nature Communications* 12(1), page 217. DOI: 10.1038/s41467-020-20354-2.

Alloway, B. V., N. J. G. Pearce, P. I. Moreno, G. Villarosa, I. A. Jara, C. A. Henríquez, E. A. Sagredo, M. T. Ryan, and V. Outes (2022). "Refinement of the tephrostratigraphy straddling the northern Patagonian Andes (40–41°S): new tephra markers, reconciling different archives and ascertaining the timing of piedmont deglaciation". *Journal of Quaternary Science* 37(3), pages 441–477. DOI: 10.1002/jqs.3389.

Anderson, A. (1976). "Magma mixing: petrological process and volcanological tool". *Journal of Volcanology and Geothermal Research* 1(1), pages 3–33. DOI: 10.1016/0377-0273(76)90016-0.

Anderson, A. T. and G. G. Brown (1993). "CO_2 contents and formation pressures of some Kilauean melt inclusions". *American Mineralogist* 78, pages 794–803.

Aster, E. M., P. J. Wallace, L. R. Moore, J. Watkins, E. Gazel, and R. J. Bodnar (2016). "Reconstructing CO2 concentrations in basaltic melt inclusions using Raman analysis of vapor bubbles". *Journal of Volcanology and Geothermal Research* 323, pages 148–162. DOI: 10.1016/j.jvolgeores.2016.04.028.

Audétat, A. and J. Lowenstern (2014). "Melt Inclusions". *Treatise on Geochemistry*. Elsevier, pages 143–173. ISBN: 978-0-08-098300-4. DOI: 10.1016/B978-0-08-095975-7.01106-2.

Barker, S. J., M. C. Rowe, C. J. Wilson, J. A. Gamble, S. M. Rooyakkers, R. J. Wysoczanski, F. Illsley-Kemp, and C. C. Kenworthy (2020). "What lies beneath? Reconstructing the primitive magmas fueling voluminous silicic volcanism using olivine-hosted melt inclusions". *Geology* 48(5), pages 504–508. DOI: 10.1130/G47422.1.

Bertrand, S., J. Castiaux, and E. Juvigné (2008). "Tephrostratigraphy of the late glacial and Holocene sediments of Puyehue Lake (Southern Volcanic Zone, Chile, 40°S)". *Quaternary Research* 70(3), pages 343–357. DOI: 10.1016/j.yqres.2008.06.001.

Beucher, S. and C. Lantuéjoul (1979). "Use of Watersheds in Contour Detection". *International Workshop on Image Processing*.

Beucher, S. and F. Meyer (1993). "The morphological approach to segmentation: the watershed transformation". *Mathematical morphology in image processing*. Marcel Dekker Inc., New York, pages 433–481. DOI: 10.1201/9781482277234-12.

Brahm, R., G. F. Zellmer, T. Kuritani, D. C. Jr., M. Nakagawa, N. Sakamoto, H. Yurimoto, and E. Sato (2021). "MushPEC: Correcting Post-entrapment Processes Affecting Melt Inclusions Hosted in Olivine Antecrysts". *Frontiers in Earth Science* 8, page 599726. DOI: 10.3389/feart.2020.599726.

Buso, R., D. Laporte, F. Schiavi, N. Cluzel, and C. Fonquernie (2022). "High-Pressure Homogenization of Olivine-Hosted CO2-Rich Melt Inclusions in a Piston Cylinder: Insight into the Volatile Content of Primary Mantle Melts". *European Journal of Mineralogy* 34(3), pages 325–349. DOI: 10.5194/ejm-34-325-2022.

Cannatelli, C., A. Doherty, R. Esposito, A. Lima, and B. De Vivo (2016). "Understanding a volcano through a droplet: A melt inclusion approach". *Journal of Geochemical Exploration* 171, pages 4–19. DOI: 10.1016/j.gexplo.2015.10.003.

Cnudde, V. and M. Boone (2013). "High-resolution X-ray computed tomography in geosciences: A review of the current technology and applications". *Earth-Science Reviews* 123, pages 1–17. DOI: 10.1016/j.earscirev.2013.04.003.

Créon, L., G. Levresse, L. Remusat, H. Bureau, and G. Carrasco-Núñez (2018). "New method for initial composition determination of crystallized silicate melt inclusions". *Chemical Geology* 483, pages 162–173. DOI: 10.1016/j.chemgeo.2018.02.038.

Danyushevsky, L. V., F. N. Della-Pasqua, and S. Sokolov (2000). "Re-equilibration of melt inclusions trapped by magnesian olivine phenocrysts from subduction-related magmas: petrological implications". *Contributions to Mineralogy and Petrology* 138(1), pages 68–83. DOI: 10.1007/PL00007664.

Danyushevsky, L. V., A. W. McNeill, and A. V. Sobolev (2002). "Experimental and petrological studies of melt inclusions in phenocrysts from mantle-derived magmas: an overview of techniques, advantages and complications". *Chemical Geology* 183(1–4), pages 5–24. DOI: 10.1016/s0009-2541(01)00369-2.

DeVitre, C. L., C. M. Allison, and E. Gazel (2021). "A high-precision CO2 densimeter for Raman spectroscopy using a

Fluid Density Calibration Apparatus". *Chemical Geology* 584, page 120522. DOI: 10.1016/j.chemgeo.2021.120522.

DeVitre, C. L., E. Gazel, R. S. Ramalho, S. Venugopal, M. Steele-MacInnis, J. Hua, C. M. Allison, L. R. Moore, J. C. Carracedo, and B. Monteleone (2023). "Oceanic intraplate explosive eruptions fed directly from the mantle". *Proceedings of the National Academy of Sciences of the United States of America* 120(33), e2302093120. DOI: 10.1073/pnas.2302093120.

Esposito, R., R. J. Bodnar, L. V. Danyushevsky, B. De Vivo, L. Fedele, J. Hunter, A. Lima, and N. Shimizu (2011). "Volatile Evolution of Magma Associated with the Solchiaro Eruption in the Phlegrean Volcanic District (Italy)". *Journal of Petrology* 52(12), pages 2431–2460. DOI: 10.1093/petrology/egr051.

Esposito, R., J. Hunter, J. D. Schiffbauer, N. Shimizu, and R. J. Bodnar (2014). "An assessment of the reliability of melt inclusions as recorders of the pre-eruptive volatile content of magmas". *American Mineralogist* 99(5-6), pages 976–998. DOI: 10.2138/am.2014.4574.

Esposito, R., K. Badescu, J. W. Boyce, and M.-L. Frezzotti (2023). "Chemical characterization of a magma recharging and mixing before an eruption: Insights from chronologically constrained melt inclusions". *Lithos* 456-457, page 107301. DOI: 10.1016/j.lithos.2023.107301.

Feignon, J.-G., N. Cluzel, F. Schiavi, S. Moune, O. Roche, J. Clavero, P. Schiano, and M. Auxerre (2022). "High CO2 content in magmas of the explosive andesitic Enco eruption of Mocho-Choshuenco volcano (Chile)". *Bulletin of Volcanology* 84(4), page 40. DOI: 10.1007/s00445-022-01550-y.

Fontijn, K., H. Rawson, M. Van Daele, J. Moernaut, A. M. Abarzúa, K. Heirman, S. Bertrand, D. M. Pyle, T. A. Mather, M. De Batist, J.-A. Naranjo, and H. Moreno (2016). "Synchronisation of sedimentary records using tephra: A post-glacial tephrochronological model for the Chilean Lake District". *Quaternary Science Reviews* 137, pages 234–254. DOI: 10.1016/j.quascirev.2016.02.015.

Glasser, N. F., K. N. Jansson, S. Harrison, and J. Kleman (2008). "The glacial geomorphology and Pleistocene history of South America between 38°S and 56°S". *Quaternary Science Reviews* 27(3-4), pages 365–390. DOI: 10.1016/j.quascirev.2007.11.011.

Hanyu, T., J. Yamamoto, K. Kimoto, K. Shimizu, and T. Ushikubo (2020). "Determination of total CO2 in melt inclusions with shrinkage bubbles". *Chemical Geology* 557, page 119855. DOI: 10.1016/j.chemgeo.2020.119855.

Hartley, M. E., J. Maclennan, M. Edmonds, and T. Thordarson (2014). "Reconstructing the deep CO2 degassing behaviour of large basaltic fissure eruptions". *Earth and Planetary Science Letters* 393, pages 120–131. DOI: 10.1016/j.epsl.2014.02.031.

Hulton, N., R. Purves, R. McCulloch, D. Sugden, and M. Bentley (2002). "The Last Glacial Maximum and deglaciation in southern South America". *Quaternary Science Reviews* 21(1-3), pages 233–241. DOI: 10.1016/S0277-3791(01)00103-2.

Jackson, M. and S. Hart (2006). "Strontium isotopes in melt inclusions from Samoan basalts: Implications for heterogeneity in the Samoan plume". *Earth and Planetary Science Letters* 245(1-2), pages 260–277. DOI: 10.1016/j.epsl.2006.02.040.

Jorgenson, C., M. E. Stuckelberger, G. Fevola, G. Falkenberg, T. Kaiser, F. Wilde, G. Weber, G. Giordano, and L. Caricchi (2025). "A Myriad of Melt Inclusions: A 3D Analysis of Melt Inclusions Reveals the Gas-Rich Magma Reservoir of Colli Albani Volcano (Italy)". *Journal of Petrology* 66. Advance Access publication date 6 February 2025, egaf012. DOI: 10.1093/petrology/egaf012.

Lamadrid, H., L. Moore, D. Moncada, J. Rimstidt, R. Burruss, and R. Bodnar (2017). "Reassessment of the Raman CO_2 densimeter". *Chemical Geology* 450, pages 210–222. DOI: 10.1016/j.chemgeo.2016.12.034.

Laumonier, M., D. Laporte, F. Faure, A. Provost, P. Schiano, and K. Ito (2019). "An experimental study of dissolution and precipitation of forsterite in a thermal gradient: implications for cellular growth of olivine phenocrysts in basalt and melt inclusion formation". *Contributions to Mineralogy and Petrology* 174(11), page 94. DOI: 10.1007/s00410-019-1627-x.

Lin, Q., S. Neethling, K. Dobson, L. Courtois, and P. Lee (2015). "Quantifying and minimising systematic and random errors in X-ray micro-tomography based volume measurements". *Computers & Geosciences* 77, pages 1–7. DOI: 10.1016/j.cageo.2014.12.008.

Lopez, T., T. P. Fischer, T. Plank, A. Malinverno, A. L. Rizzo, D. J. Rasmussen, E. Cottrell, C. Werner, C. Kern, D. Bergfeld, T. Ilanko, J. L. Andrys, and K. A. Kelley (2023). "Tracking carbon from subduction to outgassing along the Aleutian-Alaska Volcanic Arc". *Science Advances* 9(26), eadf3024. DOI: 10.1126/sciadv.adf3024.

Lowenstern, J. B. (1995). "Applications of silicate melt inclusions to study magmatic volatiles". *Magmas, Fluids and Ore Deposits*. Volume 23. Short course series. Mineralogical Association of Canada, pages 71–99. ISBN: 0-921294-00-X.

– (2003). "Melt inclusions come of age: Volatiles, volcanoes, and sorby's legacy". *Developments in Volcanology*. Volume 5. Elsevier, pages 1–21. ISBN: 978-0-444-51151-5. DOI: 10.1016/S1871-644X(03)80021-9.

Maclennan, J. (2017). "Bubble formation and decrepitation control the CO $_2$ content of olivine-hosted melt inclusions". *Geochemistry, Geophysics, Geosystems* 18(2), pages 597–616. DOI: 10.1002/2016GC006633.

Mallea-Lillo, F. (2022). "Contrasting sources and conditions of shallow magmatic reservoirs of the Fui Group small eruptive centres associated with the Liquiñe-Ofqui Fault Zone (Chilean Andes)". *Journal of South American Earth Sciences*, page 18. DOI: 10.1016/j.jsames.2022.103875.

Mann, C. P., P. J. Wallace, and J. Stix (2013). "Phenocryst-hosted melt inclusions record stalling of magma during ascent in the conduit and upper magma reservoir prior to vulcanian explosions, Soufrière Hills volcano, Montserrat, West Indies". *Bulletin of Volcanology* 75(2), page 687. DOI: 10.1007/s00445-013-0687-4.

McMillan, N. J., R. S. Harmon, S. Moorbath, L. Lopez-Escobar, and D. F. Strong (1989). "Crustal sources involved in continental arc magmatism: A case study of volcan Mocho-

Choshuenco, southern Chile". *Geology* 17(12), page 1152. DOI: 10.1130/0091-7613(1989)017<1152:CSIICA>2.3.CO;2.

Metrich, N. and P. J. Wallace (2008). "Volatile Abundances in Basaltic Magmas and Their Degassing Paths Tracked by Melt Inclusions". *Reviews in Mineralogy and Geochemistry* 69(1), pages 363–402. DOI: 10.2138/rmg.2008.69.10.

Miller, W. G., J. Maclennan, O. Shorttle, G. A. Gaetani, V. Le Roux, and F. Klein (2019). "Estimating the carbon content of the deep mantle with Icelandic melt inclusions". *Earth and Planetary Science Letters* 523, page 115699. DOI: 10.1016/j.epsl.2019.07.002.

Mironov, N., D. Tobelko, S. Smirnov, M. Portnyagin, and S. Krasheninnikov (2020). "Estimation of CO2 Content in the Gas Phase of Melt Inclusions Using Raman Spectroscopy: Case Study of Inclusions in Olivine from the Karymsky Volcano (Kamchatka)". *Russian Geology and Geophysics* 61(5–6), pages 600–610. DOI: 10.15372/RGG2019169.

Mironov, N., M. Portnyagin, R. Botcharnikov, A. Gurenko, K. Hoernle, and F. Holtz (2015). "Quantification of the CO 2 budget and H 2 O–CO 2 systematics in subduction-zone magmas through the experimental hydration of melt inclusions in olivine at high H 2 O pressure". *Earth and Planetary Science Letters* 425, pages 1–11. DOI: 10.1016/j.epsl.2015.05.043.

Moore, L. R., E. Gazel, R. Tuohy, A. S. Lloyd, R. Esposito, M. Steele-MacInnis, E. H. Hauri, P. J. Wallace, T. Plank, and R. J. Bodnar (2015). "Bubbles matter: An assessment of the contribution of vapor bubbles to melt inclusion volatile budgets". *American Mineralogist* 100(4), pages 806–823. DOI: 10.2138/am-2015-5036.

Moreno-Yaeger, P., B. S. Singer, B. R. Edwards, B. R. Jicha, W. O. Nachlas, M. D. Kurz, R. E. Breunig, I. Fustos-Toribio, D. V. Antipán, and E. Piergrossi (2024). "Pleistocene to recent evolution of Mocho-Choshuenco volcano during growth and retreat of the Patagonian Ice Sheet". *Geological Society of America Bulletin* 136(11–12), pages 5262–5282. DOI: 10.1130/b37514.1.

Mourey, A. J. and T. Shea (2019). "Forming Olivine Phenocrysts in Basalt: A 3D Characterization of Growth Rates in Laboratory Experiments". *Frontiers in Earth Science* 7, page 300. DOI: 10.3389/feart.2019.00300.

Nakashima, Y., H. Hirai, A. Koishikawa, and T. Ohtani (1997). "Three-dimensional imaging of arrays of fluid inclusions in fluorite by high-resolution X-ray CT". *Neues Jahrbuch für Mineralogie* 1997(12), pages 559–568. DOI: 10.1127/njmm/1997/1997/559.

Neave, D. A., J. Maclennan, M. Edmonds, and T. Thordarson (2014). "Melt mixing causes negative correlation of trace element enrichment and CO2 content prior to an Icelandic eruption". *Earth and Planetary Science Letters* 400, pages 272–283. DOI: 10.1016/j.epsl.2014.05.050.

Newcombe, M. E., A. Fabbrizio, Y. Zhang, C. Ma, M. Le Voyer, Y. Guan, J. M. Eiler, A. E. Saal, and E. M. Stolper (2014). "Chemical zonation in olivine-hosted melt inclusions". *Contributions to Mineralogy and Petrology* 168(1), page 1030. DOI: 10.1007/s00410-014-1030-6.

Newman, S. and J. B. Lowenstern (2002). "VolatileCalc: a silicate melt–H2O–CO2 solution model written in Visual Basic for excel". *Computers & Geosciences* 28(5), pages 597–604. DOI: 10.1016/S0098-3004(01)00081-4.

Ni, P., Y. Zhang, and Y. Guan (2017). "Volatile loss during homogenization of lunar melt inclusions". *Earth and Planetary Science Letters* 478, pages 214–224. DOI: https://doi.org/10.1016/j.epsl.2017.09.010.

Pamukcu, A. S., G. A. R. Gualda, and M. L. Rivers (2013). "Quantitative 3D petrography using X-ray tomography 4: Assessing glass inclusion textures with propagation phase-contrast tomography". *Geosphere* 9(6), pages 1704–1713. DOI: 10.1130/GES00915.1.

Pamukcu, A. S., G. A. Gualda, F. Bégué, and D. M. Gravley (2015). "Melt inclusion shapes: Timekeepers of short-lived giant magma bodies". *Geology* 43(11), pages 947–950. DOI: 10.1130/G37021.1.

Pan, V., J. R. Holloway, and R. L. Hervig (1991). "The pressure and temperature dependence of carbon dioxide solubility in tholeiitic basalt melts". *Geochimica et Cosmochimica Acta* 55(6), pages 1587–1595. DOI: 10.1016/0016-7037(91)90130-W.

Pankhurst, M. J., K. J. Dobson, D. J. Morgan, S. C. Loughlin, T. Thordarson, P. D. Lee, and L. Courtois (2014). "Monitoring the Magmas Fuelling Volcanic Eruptions in Near-real-time Using X-ray Micro-computed Tomography". *Journal of Petrology* 55(3), pages 671–684. DOI: 10.1093/petrology/egt079.

Perona, P. and J. Malik (1990). "Scale-space and edge detection using anisotropic diffusion". *IEEE Transactions on Pattern Analysis and Machine Intelligence* 12(7), pages 629–639. DOI: 10.1109/34.56205.

Plank, T., K. A. Kelley, M. M. Zimmer, E. H. Hauri, and P. J. Wallace (2013). "Why do mafic arc magmas contain ~4wt% water on average?" *Earth and Planetary Science Letters* 364, pages 168–179. DOI: 10.1016/j.epsl.2012.11.044.

Plank, T. and C. E. Manning (2019). "Subducting carbon". *Nature* 574(7778), pages 343–352. DOI: 10.1038/s41586-019-1643-z.

Rasmussen, D. J., T. A. Plank, P. J. Wallace, M. E. Newcombe, and J. B. Lowenstern (2020). "Vapor-bubble growth in olivine-hosted melt inclusions". *American Mineralogist* 105(12), pages 1898–1919. DOI: 10.2138/am-2020-7377.

Rawson, H., T. Keller, K. Fontijn, D. M. Pyle, T. A. Mather, V. C. Smith, and J. A. Naranjo (2016a). "Compositional variability in mafic arc magmas over short spatial and temporal scales: Evidence for the signature of mantle reactive melt channels". *Earth and Planetary Science Letters* 456, pages 66–77. DOI: 10.1016/j.epsl.2016.09.056.

Rawson, H., J. A. Naranjo, V. C. Smith, K. Fontijn, D. M. Pyle, T. A. Mather, and H. Moreno (2015). "The frequency and magnitude of post-glacial explosive eruptions at Volcán Mocho-Choshuenco, southern Chile". *Journal of Volcanology and Geothermal Research* 299, pages 103–129. DOI: 10.1016/j.jvolgeores.2015.04.003.

Rawson, H., D. M. Pyle, T. A. Mather, V. C. Smith, K. Fontijn, S. M. Lachowycz, and J. A. Naranjo (2016b). "The magmatic and eruptive response of arc volcanoes to deglaciation: In-

sights from southern Chile". *Geology* 44(4), pages 251–254. DOI: 10.1130/G37504.1.

Richard, A., C. Morlot, L. Créon, N. Beaudoin, V. S. Balistky, S. Pentelei, V. Dyja-Person, G. Giuliani, I. Pignatelli, H. Legros, J. Sterpenich, and J. Pironon (2019). "Advances in 3D imaging and volumetric reconstruction of fluid and melt inclusions by high resolution X-ray computed tomography". *Chemical Geology* 508, pages 3–14. DOI: 10.1016/j.chemgeo.2018.06.012.

Roedder, E. (1979). "Origin and significance of magmatic inclusions". *Bulletin de Minéralogie* 102(5), pages 487–510. DOI: 10.3406/bulmi.1979.7299.

Roerdink, J. B. and A. Meijster (2001). "The Watershed Transform: Definitions, Algorithms and Parallelization Strategies". *Fundamenta Informaticae* 41(3-4), pages 187–228. DOI: 10.3233/FI-2000-411207.

Rose-Koga, E., A.-S. Bouvier, G. Gaetani, P. Wallace, C. Allison, J. Andrys, C. Angeles de la Torre, A. Barth, R. Bodnar, A. Bracco Gartner, D. Butters, A. Castillejo, B. Chilson-Parks, B. Choudhary, N. Cluzel, M. Cole, E. Cottrell, A. Daly, L. Danyushevsky, C. DeVitre, M. Drignon, L. France, M. Gaborieau, M. Garcia, E. Gatti, F. Genske, M. Hartley, E. Hughes, A. Iveson, E. Johnson, M. Jones, T. Kagoshima, Y. Katzir, M. Kawaguchi, T. Kawamoto, K. Kelley, J. Koornneef, M. Kurz, M. Laubier, G. Layne, A. Lerner, K.-Y. Lin, P.-P. Liu, A. Lorenzo-Merino, N. Luciani, N. Magalhães, H. Marschall, P. Michael, B. Monteleone, L. Moore, Y. Moussallam, M. Muth, M. Myers, D. Narváez, O. Navon, M. Newcombe, A. Nichols, R. Nielsen, A. Pamukcu, T. Plank, D. Rasmussen, J. Roberge, F. Schiavi, D. Schwartz, K. Shimizu, K. Shimizu, N. Shimizu, J. Thomas, G. Thompson, J. Tucker, G. Ustunisik, C. Waelkens, Y. Zhang, and T. Zhou (2021). "Silicate melt inclusions in the new millennium: A review of recommended practices for preparation, analysis, and data presentation". *Chemical Geology* 570, pages 120–145. DOI: 10.1016/j.chemgeo.2021.120145.

Rose-Koga, E., K. Koga, M. Moreira, I. Vlastelic, M. Jackson, M. Whitehouse, N. Shimizu, and N. Habib (2017). "Geochemical systematics of Pb isotopes, fluorine, and sulfur in melt inclusions from São Miguel, Azores". *Chemical Geology* 458, pages 22–37. DOI: 10.1016/j.chemgeo.2017.03.024.

Rose-Koga, E. F., K. T. Koga, P. Schiano, M. Le Voyer, N. Shimizu, M. J. Whitehouse, and R. Clocchiatti (2012). "Mantle source heterogeneity for South Tyrrhenian magmas revealed by Pb isotopes and halogen contents of olivine-hosted melt inclusions". *Chemical Geology* 334, pages 266–279. DOI: 10.1016/j.chemgeo.2012.10.033.

Schlüter, S., A. Sheppard, K. Brown, and D. Wildenschild (2014). "Image processing of multiphase images obtained via X-ray microtomography: A review". *Water Resources Research* 50(4), pages 3615–3639. DOI: 10.1002/2014WR015256.

Shishkina, T. A., R. E. Botcharnikov, F. Holtz, R. R. Almeev, A. M. Jazwa, and A. A. Jakubiak (2014). "Compositional and pressure effects on the solubility of H2O and CO2 in mafic melts". *Chemical Geology* 388, pages 112–129. DOI: 10.1016/j.chemgeo.2014.09.001.

Steele-MacInnis, M., R. Esposito, L. R. Moore, and M. E. Hartley (2017). "Heterogeneously entrapped, vapor-rich melt inclusions record pre-eruptive magmatic volatile contents". *Contributions to Mineralogy and Petrology* 172(4), page 18. DOI: 10.1007/s00410-017-1343-3.

Stolper, E. and D. Walker (1980). "Melt Density and the Average Composition of Basalt". *Contributions to Mineralogy and Petrology* 74, pages 7–12. DOI: 10.1007/BF00375492.

Tucker, J. M., E. H. Hauri, A. J. Pietruszka, M. O. Garcia, J. P. Marske, and F. A. Trusdell (2019). "A high carbon content of the Hawaiian mantle from olivine-hosted melt inclusions". *Geochimica et Cosmochimica Acta* 254, pages 156–172. DOI: 10.1016/j.gca.2019.04.001.

Van Gerve, T. D., D. A. Neave, P. Wieser, H. Lamadrid, N. Hulsbosch, and O. Namur (2024). "The Origin and Differentiation of CO 2 -Rich Primary Melts in Ocean Island Volcanoes: Integrating 3D X-Ray Tomography with Chemical Microanalysis of Olivine-Hosted Melt Inclusions from Pico (Azores)." *Journal of Petrology* 65(2), egae006. DOI: 10.1093/petrology/egae006.

Venugopal, S., F. Schiavi, S. Moune, N. Bolfan-Casanova, T. Druitt, and G. Williams-Jones (2020). "Melt inclusion vapour bubbles: the hidden reservoir for major and volatile elements". *Scientific Reports* 10(1), page 9034. DOI: 10.1038/s41598-020-65226-3.

Wallace, P. J., V. S. Kamenetsky, and P. Cervantes (2015). "Melt inclusion CO2 contents, pressures of olivine crystallization, and the problem of shrinkage bubbles". *American Mineralogist* 100(4), pages 787–794. DOI: 10.2138/am-2015-5029.

Wallace, P. J. (2005). "Volatiles in subduction zone magmas: concentrations and fluxes based on melt inclusion and volcanic gas data". *Journal of Volcanology and Geothermal Research* 140(1–3), pages 217–240. DOI: 10.1016/j.jvolgeores.2004.07.023.

Wallace, P. J., T. Plank, R. J. Bodnar, G. A. Gaetani, and T. Shea (2021). "Olivine-Hosted Melt Inclusions: A Microscopic Perspective on a Complex Magmatic World". *Annual Review Earth and Planetary Sciences* 49(1), pages 465–494. DOI: 10.1146/annurev-earth-082420-060506.

Welsch, B., J. Hammer, and E. Hellebrand (2014). "Phosphorus zoning reveals dendritic architecture of olivine". *Geology* 42(10), pages 867–870. DOI: 10.1130/G35691.1.

Wieser, P. E., H. Lamadrid, J. Maclennan, M. Edmonds, S. Matthews, K. Iacovino, F. E. Jenner, C. Gansecki, F. Trusdell, R. Lee, and E. Ilyinskaya (2021). "Reconstructing Magma Storage Depths for the 2018 Kılauean Eruption From Melt Inclusion CO $_2$ Contents: The Importance of Vapor Bubbles". *Geochemistry, Geophysics, Geosystems* 22(2). DOI: 10.1029/2020GC009364.

Withers, P. J., C. Bouman, S. Carmignato, V. Cnudde, D. Grimaldi, C. K. Hagen, E. Maire, M. Manley, A. Du Plessis, and S. R. Stock (2021). "X-ray computed tomography". *Nature Reviews Methods Primers* 1(1), page 18. DOI: 10.1038/s43586-021-00015-4.

Wong, K., E. Mason, S. Brune, M. East, M. Edmonds, and S. Zahirovic (2019). "Deep Carbon Cycling Over the Past 200 Million Years: A Review of Fluxes in Different Tectonic

Settings". *Frontiers in Earth Science* 7, page 263. DOI: 10.3389/feart.2019.00263.

Yao, Y., E. Takazawa, S. Chatterjee, A. Richard, C. Morlot, L. Créon, S. Al–Busaidi, and K. Michibayashi (2020). "High resolution X–ray computed tomography and scanning electron microscopy studies of multiphase solid inclusions in Oman podiform chromitite: implications for post–entrapment modification". *Journal of Mineralogical and Petrological Sciences* 115(3), pages 247–260. DOI: 10.2465/jmps.191008.